TUDelft

Delft University of Technology

Numerical investigation into the effects of corrosion on the shear performance of pretensioned bridge girders with cast-in-place slabs

Jadwiga Osmolska, Magdalena; Kanstad, Terje; Hendriks, Max A.N.; Markeset, Gro

Important note
To cite this publication, please use the final published version (if applicable).
Please check the document version above.

Numerical investigation into the effects of corrosion on the shear performance of pretensioned bridge girders with cast-in-place slabs

Magdalena Jadwiga Osmolska [a,b,*], Terje Kanstad [b], Max A.N. Hendriks [b,c], Gro Markeset [a]

[a] *Oslo Metropolitan University (OsloMet), Department of Civil Engineering and Energy Technology, Pilestredet 35, 0166 Oslo, Norway*
[b] *Norwegian University of Sciences and Technology (NTNU), Department of Structural Engineering, Richard Birkelandsvei 1A, 7034 Trondheim, Norway*
[c] *Delft University of Technology (TU Delft), The Netherlands*

ABSTRACT

Corrosion and shear cracking are frequently observed near supports of pretensioned bridge girders in coastal climates, so non-linear finite element analysis was used to study the effect of corrosion on shear performance in a real case study. Varying degrees of corrosion and various locations (top strands, bottom strands, vertical stirrups and girder-slab interface) were considered. The analyses included construction phases, concrete creep and shrinkage, and the effects of corrosion on the properties of prestressing and reinforcing steel, concrete, and the bond between concrete and reinforcement. The study shows that high (20%) corrosion in the bottom layer of strands can modify the failure mode from concrete crushing in the web to strand slippage or crushing of concrete in the support zone with limited cracking. Although severe strand corrosion significantly compromises girder capacity and ductility, failure occurs only when there is overloading. The predicted failure mode was also sensitive to material parameters, in particular the corrosion-induced crack widths used for modelling the reduced concrete strength. Nevertheless, some similarities were noticed between observed and predicted cracking occurrence. For moderate corrosion (10%), girder capacity was limited by strand fracture, but extensive flexure and shear cracking would appear before failure. 20% corrosion in the vertical stirrups in the web seems to have potentially smaller effect on the shear capacity than 20% corrosion in the strands in support, while corrosion in the top strands or stirrups in the girder-slab interface did not affect the girder capacity.

1. Introduction

An increasing number of cases of corrosion deterioration in aging pretensioned bridge girders have been reported, particularly in bridges exposed to aggressive marine environments or de-icing salts [1–3]. Corrosion reduces the cross-section and mechanical properties of pretensioned and ordinary reinforcement, and it induces concrete cracking and spalling causing degradation of the bond between concrete and reinforcement. Severe corrosion, in particular in the highly stressed and small-diameter wires of the strands, can lead to sudden reinforcement fracture, affecting the serviceability and load-bearing capacity of structures. To avoid catastrophic consequences, decisions need to be made on necessary repairs, strengthening or replacements based on reliable assessments of the residual capacity of corroded pretensioned girders.

Accurate prediction of the structural performance of corroded

pretensioned girders requires precise modelling of the corrosion distribution along the girder [4,5]. This information cannot be obtained without opening the concrete cover, but a durability study of pretensioned I-shaped girder bridges in Norway's coastal climate [3] has shown that girder support zones and their vicinities are particularly vulnerable to chloride-induced corrosion. Recent, experimental research on inspection and corrosion assessment in pretensioned bridge girders in a coastal climate [6] supports the above findings. The highest probability of strand corrosion in the girders investigated in Dalselv Bridge was found at a distance about 3.3 m from the middle support, while the mid-part of the span had negligible corrosion probability. High corrosion probability was also found in the vertical stirrups in the web near the supports [6]. Except for the webs and bottom flanges, severe corrosion damage was also frequently found in the top flanges of the pretensioned girders and in bridge slabs [3].

The only structural cracks reported in I-shaped pretensioned girders in bridges in Norway's coastal environment are shear cracks [3,7]. For

---

* Corresponding author at: Oslo Metropolitan University (OsloMet), Department of Civil Engineering and Energy Technology, Pilestredet 35, 0166 Oslo, Norway.
E-mail addresses: magdap@oslomet.no (M. Jadwiga Osmolska), terje.kanstad@ntnu.no (T. Kanstad), max.hendriks@ntnu.no (M.A.N. Hendriks), gromark@oslomet.no (G. Markeset).

Notation

α_y, α_u, α_1	Empirical coefficients	E_{norm}	Linear normal stiffness modulus related to the crushing of the concrete by the strand
α	Constant value	E_{shear}	Initial linear shear stiffness related to bond-slip curve
α_{p1}	Coefficient considering the type of release	E_s	Young's modulus of uncorroded pretensioning strands
α_{p2}	Coefficient considering the action effect to be verified	$E_{s.c}$	Young's modulus of corroded pretensioning strands
α_{ct}	Material coefficient	f_{bpt}	Design value of the bond strength for pretensioned strand
γ_c	Material factor for concrete	f_{cc}	Cylinder compressive strength of concrete
ε_{c0}	Concrete strain at compressive strength	$f_{cc.cracked}$	Cylinder compressive strength of cracked concrete
ε_{c1}	Average transverse strain of the cracked concrete	f_{ck}	Characteristic cylinder compressive strength of concrete
ε_{pu}	Ultimate strain of uncorroded pretensioning strands	$f_{ck.cube}$	Characteristic cube compressive strength of concrete
$\varepsilon_{pu.c}$	Ultimate strain of corroded pretensioning strands	f_{cm}	Mean compressive strength of concrete
$\varepsilon_{py.c}$	Yield strain of corroded pretensioning strands	$f_{cm.cracked}$	Mean compressive strength of cracked concrete
ε_u	Ultimate strain of uncorroded reinforcement	f_{ct}	Tensile strength of concrete
$\varepsilon_{u.c}$	Ultimate strain of corroded reinforcement	$f_{ct.cracked}$	Tensile strength of cracked concrete
η_{p1}	Coefficient taking into account the type of strand	f_{ctd}	Design tensile strength of concrete
η_1	Coefficient taking into account the position of strand	f_{ctm}	Mean tensile strength of concrete
θ	Inclination of main concrete compressive strut	$f_{ctm.cracked}$	Mean tensile strength of cracked concrete
v_{rs}	Ratio of the volumetric expansion of corrosion products compared to steel	f_{py}	Yield strength of uncorroded pretensioning strands
		$f_{py.c}$	Yield strength of corroded pretensioning strands (effective)
ρ	Corrosion degree of reinforcement	f_{pu}	Ultimate strength of uncorroded pretensioning strands
ρ_s	Corrosion degree (average) of pretensioning strands	$f_{pu.c}$	Ultimate strength of corroded pretensioning strands (effective)
σ_{pm0}	Stress in the strands just after releasing	f_u	Ultimate strength of uncorroded reinforcement
τ	Bond stress for strand	$f_{u.c}$	Ultimate strength of corroded reinforcement
τ_{max}	Maximum bond stress for uncorroded strand	f_y	Yield strength of uncorroded reinforcement
$\tau_{max.c}$	Maximum bond stress for corroded strand	$f_{y.c}$	Yield strength of corroded reinforcement
τ_f	Residual bond stress	G_F	Mode I tensile fracture energy
$\tau_{s.0}$	Bond stress at initial slip s_0	k	Coefficient related to bar roughness and diameter
χ	Corrosion penetration depth	L_{pt}	Prestress transfer length
$\emptyset$	Diameter of reinforcement	n	Number of bars in a layer
$\emptyset_{corr}$	Diameter of corroded reinforcement	P_{Rd}	Shear resistance expressed in terms of applied load
$\emptyset_s$	Diameter of strand	R	Strand radius
a	Shear span length	s_0	Initial slip
b_0	Cross-section width	s_1, s_2	Constant slip value
d	Effective height of the cross-section	s_3	Half of the distance between the concrete gear and the adjacent wire
E_c	Young's modulus of concrete		
E_{ck}	Characteristic Young's modulus of concrete	$u_{i.corr}$	Opening of each single corrosion crack
E_{cm}	Mean Young's modulus of concrete	V_R	Shear resistance
$E_{cm.cracked}$	Mean Young's modulus of cracked concrete	w_{cr}	Corrosion-induced crack width

a)   b)   c)
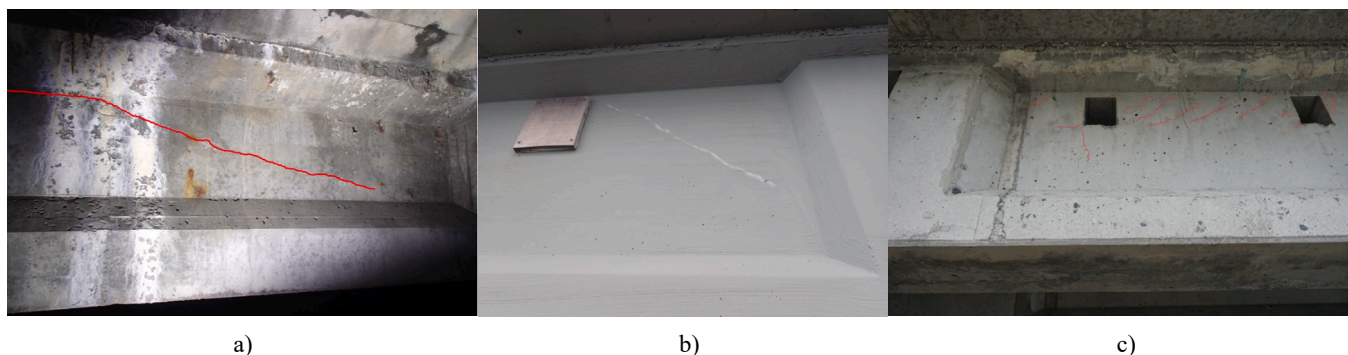
Fig. 1. Structural damage in pretensioned I-shaped bridge girders. a) Diagonal shear crack (marked in red); b) Diagonal shear crack with calcium carbonate precipitation, photo from NPRA [7]; c) Hairline diagonal cracks (marked with red) propagating from the interface between top flange and web. (For interpretation of the references to colour in this figure legend, the reader is referred to the web version of this article.)

example, an inspection made by the Norwegian Public Roads Administration (NPRA) of a bridge exposed to coastal climate for 47 years revealed a shear crack near the support in one pretensioned girder with corroding shear reinforcement. Fig. 1a shows how the diagonal shear crack propagated from the top of the web towards the bottom of the thick girder-end cross-section. A diagonal shear crack was also recently found in the outermost pretensioned girder of another bridge exposed to a harsh coastal environment for 31 years [7], see Fig. 1b. This second

bridge shows extensive corrosion in bridge slabs, and some corrosion was also found in the girders' shear reinforcement [3]. During an inspection of Dalselv Bridge made in June 2018 [6], several short and equally distributed diagonal hairline cracks were found at the top of the web near the support in the outermost girder, see Fig. 1c. Furthermore, a decrease in upward-camber was noticed in the first and second outermost pretensioned girders facing the sea, for which extensive corrosion damage was observed in the bottom and top flange near supports [6]. The above findings suggest that shear performance may be a major concern in corroded pretensioned I-shaped bridge girders.

Only a few studies in the literature have experimentally investigated the impact of corrosion in the shear span on the shear performance of pretensioned girders. The effect of corrosion in the strands and stirrups on the shear capacity was experimentally investigated on a 40-year old pretensioned girder retrieved from an I-244 bridge in Oklahoma in 2011 [8]. The corrosion was limited to the girder-end region, and the shear capacity obtained from a 3-point bending test of the full girder length with a shear span-to-depth ratio (a/d) of 1.0 was higher than required by the American Association of State Highway and Transportation Officials (AASHTO) standard specifications, AASHTO Load and Resistance Factor Design (LRFD) specifications, and the American Concrete Institute's Building Code Requirements for Structural Concrete, *ACI* 318–08 [9]. Two pretensioned girders with corroded strand-ends (retrieved from the same I-244 bridge) were also tested with an a/d ratio varying between 2.0 and 3.8 [10]. Parts of the bridge slab and concrete overlay were left intact on the top of the girder. Strand slip occurred in 2 out of 4 tests and affected the failure for high loads. Nevertheless, the shear capacity was found to be higher than calculated according to the AASHTO LRFD specifications' modified compression field theory (MCFT) procedure. Delamination and crushing of the slab overlay occurred at the end of each test and limited the girder's ultimate capacity. In Japan, pretensioned girders with bottom flange strands that were corroded and partially fractured within the shear span were experimentally tested for shear capacity [11]. The authors found that the capacity and failure mode depend on the corrosion level and distribution. Comparison with numerical and analytical calculations revealed that appropriate bond-slip and constitutive models for corroded strands should be included in the finite element analyses, while the development length of broken strands should be considered in analytical approaches.

While many studies have focused on the shear capacity of reinforced concrete (RC) beams with corroded stirrups [12–14], no research was found on the influence of stirrup corrosion on the shear capacity of pretensioned girders. Moreover, no studies seem to have investigated the effect of strand corrosion in the top flange, or corrosion of stirrups in the interface between a pretensioned girder and an RC slab. Considering the observed corrosion and structural damage in the pretensioned bridge girders described above, a lot more knowledge is needed about the shear behaviour of corroded pretensioned girders.

The main objective of this paper is to investigate the effect on the shear capacity and failure modes of pretensioned bridge girders of corrosion frequently found near supports, and the potential relationship between this corrosion damage and the shear cracks observed in the field. Due the lack of experimental tests, nonlinear finite element analysis (NLFEA) was used in this study. The analyses were performed as a case study of one standard Norwegian pretensioned (precast) I-shaped girder (NIB) with a cast-in-place RC slab, which was used in the construction of Dalselv Bridge. Since corrosion in this and other bridges was found on various parts of the girder cross-section [3,6], this paper aims to study the most probable corrosion scenarios to evaluate the effects of corrosion location (bottom flange, top flange, web, girder-slab interface) and corrosion degree on shear performance. In addition, this paper presents a review of corrosion effects on modelling the material properties and examine the impact of selected modelling parameters.

The paper is organised as follows: Section 2 provides the review of effects of corrosion on modelling the material properties; Section 3 shows details of the pretensioned girders and slabs designed for Dalselv

Bridge and analysed in this study; Section 4 contains detailed description of structural modelling and adopted methods, including validation process and details of non-linear finite element analysis; Section 5 presents the results of numerical analysis for both uncorroded and corroded girder, as well as validation and results of parametric analysis; Section 6 discussess the results, and Section 7 summarises the conclusions and provides reccomendations for further work.

2. Effect of corrosion in material models

2.1. General

Material models for uncorroded reinforcing or prestressing steel, the compressive and tensile behaviour of concrete, and the bond between the two materials need modification to account for corrosion effects. This study does not give a full literature review of the models for concrete and uncorroded steel. Concerning bond modelling, it should be noted that far fewer studies focus on the bond-slip behaviour of prestressing strands than of reinforcing bars. For instance, the fib Model Code 2010 (MC2010) [15] gives no recommendations for the bond-slip characteristics of the strands, and in the literature only the bond-slip model developed by Wang et al. [16] has been modified for corroded strands as discussed in Section 2.4 below. In what follows, we give a brief review of effects of corrosion in material modelling.

2.2. Reinforcing steel

The reduction in ductility and the related reduction in the ultimate strength of corroded reinforcement have been widely described in the literature [17–24]. In general, the bilinear elastoplastic model is commonly adopted for corroded reinforcing steel, in which the yield strength $f_{y,c}$ and ultimate strength $f_{u,c}$ are assumed to decrease linearly with increasing corrosion level, see for instance Eq. (1) and (2) proposed by Du et al. [18] and Cairns et al. [17]:

$$f_{y,c} = (1 - \alpha_y \rho) f_y \qquad (1)$$

$$f_{u,c} = (1 - \alpha_u \rho) f_u \qquad (2)$$

where f_y, and f_u are initial yield and ultimate strength respectively, ρ is the corrosion degree expressed as an average percent loss of reinforcement cross-section, while α_y and α_u, are empirical coefficients. As reported by Cairns et al. [17], the coefficients α_y and α_u may range from 0 to 0.017 and from 0 to 0.018 respectively, depending on the degree of corrosion and whether it is uniform or pitting corrosion. They found the highest values for these coefficients in chloride-exposed bars corroding in real structures. It should be noted that another study [25] suggested a slightly higher value of α_y equal to 0.020 for the corrosion degree expressed as average mass loss.

Corrosion reduces reinforcement ductility the most. As reported by Cairns et al. [17], the resulting ultimate strains can be modelled as:

$$\varepsilon_{u,c} = (1 - \alpha_1 \rho) \varepsilon_u \qquad (3)$$

where ε_u and $\varepsilon_{u,c}$ are ultimate strains for uncorroded and corroded bars respectively, and α_1 is a coefficient ranging from 0 to 0.06 with the highest values reported for pitting corrosion.

Several models for the ductility factor $\varepsilon_{u,c} / \varepsilon_u$ have also been proposed in the literature, assuming an exponential decrease with increasing corrosion degree [25] or a combination of exponential decrease with no further reduction for degrees of corrosion below and above certain values [23,24]. It should be mentioned that the actual ultimate strains of bars with similar degrees of corrosion show significant scatter within and between various studies. Besides varying bar diameter, this is mainly due to varying pitting distribution and size of the maximum pit [23].

2.3. Pretensioning strands

Previous studies of corrosion-induced degradation of the ultimate strength, ductility, and Young's modulus [26–29] of pretensioned strands have shown that the corrosion affects the ultimate strains the most, leading finally to brittle failure of the strands in the elastic stage for corrosion levels exceeding a critical value. Based on these observations, Lu et al. [26], Zhang et al. [27], Zeng et al. [28] and Wang et al. [29] proposed a constitutive model for corroded strands.

The above studies found various critical degrees of corrosion, expressed as a maximum cross-section loss of 11 % [27] and 10.4 % [29], or as an average weight loss of 8 % [26,28]. Large differences were also found among the models for the deterioration factors of mechanical properties. Zhang et al. [27] proposed deterioration of ultimate strains while Young's modulus and the effective yield strength remained intact due to small corrosion effects on those parameters. Wang et al. [29] also reported negligible effects of corrosion on Young's modulus, but proposed a model in which degradation of the effective ultimate strength was caused by stress concentration in the pit location. The most severe degradation of ultimate strength, ultimate strains and Young's modulus was proposed by Lu et al. [26]. However, all these deterioration models were derived based on the pitting corrosion area. In practice, it is difficult to locate and measure precisely the area of maximum cross-section loss in the strands.

For the average corrosion degree ρ_s, the constitutive model proposed by Zeng et al. [28] and further adapted by Tu et al. [30], may be used together with models for the reduction in effective ultimate strength $f_{pu.c}$ (calculated based on the residual cross-section area), the Young's modulus $E_{s.c}$, and ultimate strains $\varepsilon_{pu.c}$, see Eq. (4–7):

$$\sigma(\varepsilon) = \left\{ \begin{array}{c} E_{s.c}\varepsilon, \quad \varepsilon \leqslant \varepsilon_{py.c} \\ 0.85 f_{pu.c} + \left(\dfrac{0.15 f_{pu.c}}{\varepsilon_{pu.c} - \varepsilon_{py.c}} \right)(\varepsilon - \varepsilon_{py.c}), \quad \varepsilon_{py.c} < \varepsilon \leqslant \varepsilon_{pu.c} \\ E_{s.c}\varepsilon; \quad \varepsilon \leqslant \varepsilon_{pu.c} \end{array} \right\} \begin{array}{c} for \ \rho_s \leqslant 8\% \\ \\ for \ \rho_s > 8\% \end{array}$$

(4)

$$E_{s.c} = E_s(1 - 0.848\rho_s)$$

(5)

$$f_{pu.c} = \frac{f_{pu}(1 - 2.683\rho_s)}{(1 - \rho_s)}$$

(6)

$$\varepsilon_{pu.c} = \left\{ \begin{array}{c} \varepsilon_{pu}(1 - 9.387\rho_s), \rho_s \leq 8\% \\ f_{pu.c}/E_{s.c}, \rho_s > 8\% \end{array} \right.$$

(7)

where E_s, f_{pu} and ε_{pu} are the Young's modulus, ultimate strength, and strain of uncorroded strands respectively, while the $\varepsilon_{py.c} = f_{py.c} / E_{s.c}$ is the strain of corroded strands calculated for an effective yield strength of $f_{py.c} = 0.85 f_{pu.c}$. These authors also found that corrosion does not affect the Young's modulus of the wires themselves but reduces the Young's modulus of the strands. It should also be noted that they report less degradation of mechanical properties than Lu et al. [26], but more than in other similar studies [27,29].

Recently, two models [31,32] have been developed that assume a contribution from individual wires to the behaviour of each strand rather than treating the strand as a bar with an equivalent cross-section. These models consider various morphologies of the pits in wires and can accurately predict strand behaviour when the pit's details are known. However, one of the models [31] can also be used when pits in wire cannot be accurately predicted.

2.4. Bond between strands and concrete

Several studies have experimentally investigated the effect of corrosion in strands on their bond behaviour based on bending tests [33] and pull-out tests, including specimens both with stirrups [16,34,35] and without stirrups [35]. It was found that for low corrosion levels the bond strength of the strands increases due to increased friction, mechanical interlock, and concrete confinement [16,33]. When the corrosion-induced crack widths exceed the so-called critical crack width, both bond strength and stiffness deteriorate.

A critical average crack width of 0.31 mm measured over a distance of 1300 mm was reported by Wang et al. [33] for elements with stirrups, with a corresponding average corrosion degree of 5.25 % (expressed as average mass loss). Li and Yuan [34] found that a critical crack width of 0.6 mm measured over a 50 mm length degraded bond strength and stiffness. Another study by Wang et al. [16] related bond strength directly to the corrosion degree instead of crack width and found that bond strength decreases considerably at corrosion levels exceeding 6.25 %. These authors first propose a bond-slip model for uncorroded strands, which is a modification of the bond-slip model from MC2010 [15] for splitting failure ($s_1 = s_2$) with confining stirrups, see Eq. (8),

$$\tau = \left\{ \begin{array}{c} \tau_{max}\left(s/s_2\right)^\alpha, \quad 0 \leqslant s \leqslant s_2 \\ \tau_{max} - \left(\tau_{max} - \tau_f\right)\left(s - s_2/s_3 - s_2\right), \quad s_2 \leqslant s \leqslant s_3 \\ \tau_f, \quad s_3 \leqslant s \end{array} \right.$$

(8)

where τ_{max} is the maximum bond stress set equal to $1.25\sqrt{f_{ck}}$; τ_f is the residual friction stress equal to $0.4\tau_{max}$; s_2 is a constant value equal to 3 mm; s_3 is half of the distance between the concrete gear and the adjacent wires equal to 12 mm, while α is a constant value equal to 0.4. Next, for corrosion levels higher than 6 %, the authors propose a model for the degradation of the maximum bond stress:

$$\frac{\tau_{max.c}}{\tau_{max}} = \left\{ \begin{array}{c} 1.0, \quad \rho_s \leqslant 6\% \\ 2.03 e^{-0.118\rho_s}, \rho_s > 6\% \end{array} \right.$$

(9)

where $\tau_{max.c}$ is the maximum bond stress for the corroded strand; and ρ_s is the average percent corrosion of the strand.

It should be mentioned that the above empirical models given in Eq. (8–9) were derived for specimens with stirrups and a relatively low concrete compressive strength of about 35 N/mm². Nevertheless, the models were successfully used for validating the NLFEA of corroded prestressed beams with a higher concrete compressive strength of 44 N/mm² and without shear reinforcement, see Belletti et al. [5]. To take account of the lack of stirrup confinement, the authors [5] assumed residual bond stresses τ_f equal to 0.

A model for the degradation of the ultimate bond strength of strands in cracked concrete has recently been proposed by Yi et al. [36] based on characteristics of helically-twisted strands taking into account adhesion, corrosion pressure, and confinement (including varying stirrup conditions). However, the model is based on an analytical approach and its application in NLFEA is not straightforward.

2.5. Concrete

The model proposed by Coronelli and Gambarova [37] for the degradation of concrete compressive strength $f_{cc.cracked}$ due to corrosion cracking in ordinary reinforced concrete has been widely adopted to validate numerical studies of ordinary [38,39] and prestressed corroded beams [5]. The model applies the formulas:

$$f_{cc.cracked} = \frac{f_{cc}}{1 + k\frac{\varepsilon_1}{\varepsilon_{c0}}}$$

(10)

$$\varepsilon_1 = \frac{nw_{cr}}{b_0}$$

(11)

where f_{cc} is the compressive strength of uncracked concrete; k is a coefficient related to bar roughness and diameter (0.1 for medium-diameter ribbed bars [37]), and ε_{c0} is the concrete strain at
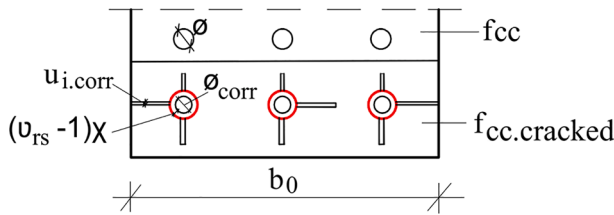
Fig. 2. Parameters for modelling the corrosion cracked concrete cover.

compressive strength. The average strain in the cracked concrete perpendicular to the direction of applied compression ε_1 is a function of the number of bars in a layer n, the cross-section width b_0, and the total crack width (for one strand) w_{cr}. For reinforced concrete, Molina et al. [40] proposed a model for estimating w_{cr}, which has since been used for pretensioned beams [5], see Eq. (12):

$$w_{cr} = \Sigma u_{i.corr} = 2\pi(\nu_{rs} - 1)\chi \tag{12}$$

where $u_{i.corr}$ is the opening of each single corrosion crack; ν_{rs} is the ratio of the volumetric expansion of corrosion products in relation to steel, which varies between 1.7 and 6.15 [40]; and χ is the corrosion penetration depth calculated from Eq. (13):

$$\chi = \frac{\varnothing - \varnothing_{corr}}{2} \tag{13}$$

where $\varnothing$ and $\varnothing_{corr}$ are the diameters of uncorroded and corroded bars respectively. The main parameters of models are illustrated in Fig. 2. Although the recommended value of ν_{rs} equal to 2.0 [40] has been widely accepted for numerical analyses of ordinary reinforced structures [38], the average value of 2.78 has been suggested for strands [41]. Even more advanced models have been proposed in the literature [41,42] to calculate crack widths in corroded pretensioned reinforcement,

considering the actual shape of the strands, the triangular shape of the cracks, and both the crack initiation and propagation stages, and corrosion filling the pores and cracks. Nevertheless, both these models are based on the thick cylinder theory and do not include multiple strands, so the calculated crack width may not necessarily correspond to reality. For estimating compressive strength rather than crack widths, the Molina et al. [40] model is therefore to be preferred.

In addition to the degradation of compressive strength, the stiffness and tensile strength of the cracked concrete will also be degraded. The stiffness can be calculated directly from the compressive strength using e.g., the expression in MC2010 [15], and the simplified assumption from previous studies [5,38,39] can be used to calculate the tensile strength $f_{ct.cracked}$, see Eq. (14):

$$f_{ct.cracked} = \frac{f_{cc.cracked}}{f_{cc}}f_{ct} \tag{14}$$

where f_{ct} is a tensile strength of uncracked concrete.

3. Details of the standard pretensioned girders and slabs designed for Dalselv bridge

Dalselv Bridge is a 40 m long two-span bridge located on the coast of northern Norway. Each of the spans consists of nine 800 mm high standard NIB girders supported through neoprene bearing pads on the abutments and the middle support. Fig. 3 shows the side view and cross-section of one NIB girder. The RC slab is continuously reinforced above the middle support and finished with a 30 mm thick concrete overlay. Although the NIB girders are I-shaped, their cross-section becomes almost rectangular at a distance of 1340 mm from the girder-ends.

The NIB girders were made of concrete strength class C55, while lower C35 class concrete was used for the cast-in-place RC slabs [43]. These concrete classes follow an old Norwegian concrete notation indicating the characteristic compressive cube strengths of 55 and 35 N/
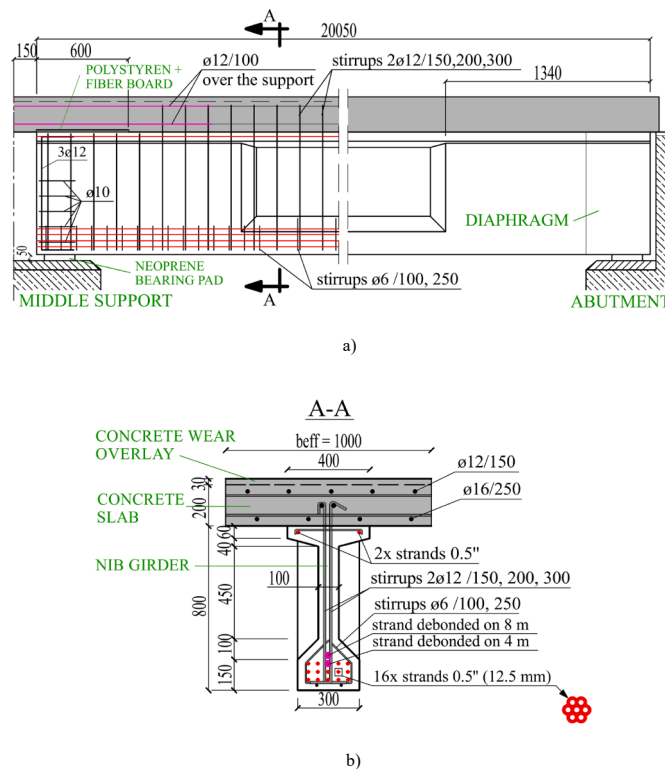

a)

b)

Fig. 3. Geometry and reinforcement arrangement in one standard I-shaped pretensioned girder (NIB) and RC slab in Dalselv Bridge, dimensions in mm, a) side view b) cross-section A-A.

Table 1
Concrete properties of the NIB girder and RC slab.

Concrete class according to NS 3473 [44,45]	C55	C35
Characteristic cube compressive strength $f_{ck.cube}$, N/mm^2	55	35
Characteristic cylinder compressive strength f_{ck}, N/mm^2	44 [1]	28 [1]
Mean cylinder compressive strength f_{cm}, N/mm^2	52 [2]	36 [2]
Young's modulus E_c at concrete age of 28 days, N/mm^2	29,563 [3]	25,814 [3]
	31,083 [4]	27,836 [4]

[1] approximately 80 % of $f_{ck.cube}$; [2] calculated according to MC2010 [15]; [3] calculated based on f_{ck} according to NS 3473 [45]: $E_{ck} = 9500 f_{ck}^{0.3}$; [4] calculated according to NS 3473 [45] by replacing f_{ck} with f_{cm}.

mm^2 respectively [44]. The remaining concrete properties were calculated according to the Norwegian Standard NS 3473 [45] and Model Code 2010 [15], considering that the characteristic cylinder strength typically corresponds to about 80 % of the cube strength, see Table 1.

As shown in Fig. 3b, sixteen pretensioning strands with a diameter of 0.5″ (12.7 mm) were located in the girder bottom flange, two of which were debonded with a flexible sheeting over a distance of 4 and 8 m from the girder ends [43]. In addition, two strands were located in the top flange. The strands were pretensioned with a force of 134 kN and 126.5 kN each in the bottom and top flange respectively, and released when the concrete compressive strength had reached 70 % of the 28-day compressive strength [46]. The ordinary reinforcement consists of ø12 vertical stirrups, ø6 stirrups confining the strands in the flanges, ø10 horizontal stirrups, and longitudinal bars in the RC slab. Depending on the bar diameter, the ordinary reinforcement was made of Ks40S/Ks40 and Ks50S steel (yield strength of 40 and 50 kp/mm^2 respectively [47]), while the strands were made of high-strength steel St 170/190 (yield strength f_{py}/ ultimate strength f_{pu}, in kp/mm^2). Table 2 shows the properties of all types of reinforcement.

Except for the middle support zone, the vertical stirrups were extended from the NIB girders and anchored to the RC slabs to enhance the composite action between the two, see Fig. 3. To distribute cracking of the slab above the middle support, the stiffness of the girder-slab connection was removed by placing thin polystyrene and fibreboard between girder and slab. This solution provided a partially continuous bridge deck system.

4. Structural modelling of pretensioned girders and methods

To investigate the effect of corrosion on the shear performance of the pretensioned NIB girders of Dalselv Bridge, we used Diana 10.5 to conduct 2-dimensional NLFEAs of both uncorroded and corroded girders with RC slabs, assuming a 3-point loaded system with sustained light traffic load of 3 kN/m. Since shear cracks were found exclusively in the thin part of the girder web near supports, see Fig. 1, the loading point was also positioned above the I-shaped part of the girder to predict those cracks. The distance of the loading point to the geometrical discontinuity of NIB girder (transition from I-shape to rectangular section) was selected as equal to the effective height of the cross-section (1d).

Corrosion was modelled only near the middle support, which is where the most severe corrosion damage occurs in real structures [6].
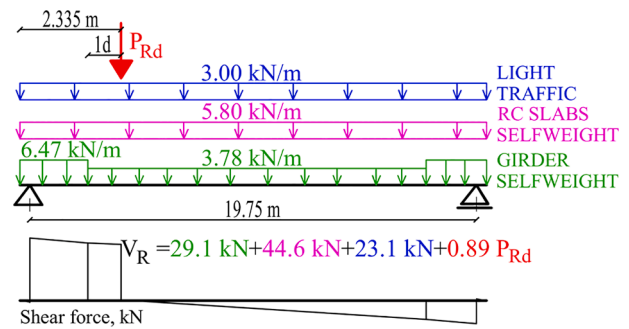

Fig. 4. Shear resistance expressed in terms of applied loads.

We investigate a total of four corrosion scenarios, as described in Section 4.1. The details of the NLFEA modelling are shown in Section 4.2.

To validate the numerical analyses, the maximum failure load obtained for an uncorroded girder was compared to the load P_{Rd}, which was analytically calculated based on shear resistance V_R and loads considered in NLFEA as shown in Fig. 4. The shear resistance V_R was determined based on Eurocode 2 (EC2) [48] and the Norwegian Standard NS 3473: 1989 [45], and assuming mean concrete compressive strength for concrete f_{cm} and characteristic yield strength for reinforcing steel f_y. The compressive stresses in the concrete due to axial load were calculated for the prestressing force including only active strands in the cross-section checked. The details of the validation are given in Section 5.2.

In addition, to estimate the margin of safety for the corroded girders, their maximum failure loads were compared to the maximum load resulting from the design loads. The design loads (multiplied by load factors) were estimated based on NPRA regulations [49], considering self-weight and equivalent traffic loads (the evenly distributed load and axle loads from heavy vehicles), the distribution of which was calculated based on unfavourable locations along and across the bridge deck, see Fig. 5. Since the design load distribution differs from NLFEA, the resulting maximum load of about 350 kN in the girder support was applied as a conservative estimation.

4.1. Corrosion scenarios

Four main corrosion scenarios CS1-CS4 were chosen to examine the effect of corrosion in individual parts of the girder cross-section on the shear performance, see Fig. 6. Considering the large amount of damage found in the girder bottom surface [6], corrosion in the most exposed bottom layer of the strands was assumed in scenario CS1, see Fig. 6a. As shown in Fig. 6b, scenario CS2 considers only corrosion of the stirrups, while corrosion of the top strands was included in CS3, see Fig. 6c. The corrosion in the girder-slab interface was investigated in CS4 by assuming the corrosion of parts of stirrups extended to the RC plate (marked with orange colour in Fig. 6d).

Since the actual degree of corrosion for individual strands cannot be found from the non-destructive test methods used in bridge inspections [6], moderate and high average corrosion of 10 % and 20 % respectively
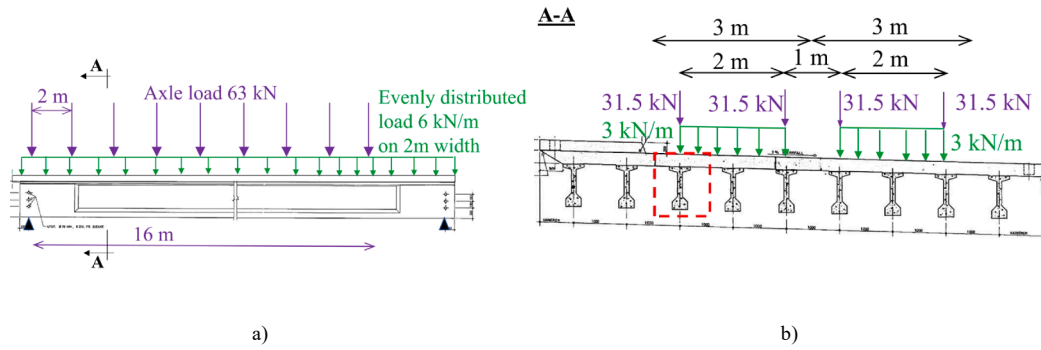
Table 2
Cross-section and material properties of pretensioned and ordinary reinforcement.

	Nominal cross section A_0 [mm^2]	Steel [43]	Yield strength [N/mm^2]	Ultimate strength [N/mm^2]	Young's Modulus [N/mm^2] [44]	Ultimate strains
Strand ø1/2″	93.7 [43]	St 170/190	1667 [1]	1863 [1]	195 000	
Bar ø6/ø10/ø12	28.3/78.5/113.1	Ks40/40S	390 [1]	490 [2]	210 000	0.15 [3]
Bar ø16	201.1	Ks50S	490 [1]	613 [2]	210 000	0.12 [3]

[1] values calculated considering that 1kp is equal to 9.807 N; [2] required by Norwegian Standard NS 481–2 minimum values calculated as 1.25 times the specified yield strength [47]; [3] minimum values specified by Norwegian Standard NS 481–2 [47]

Fig. 5. Distribution of equivalent traffic loads according to NPRA regulations. a) along the bridge deck, b) across the bridge deck, considering two traffic lanes.
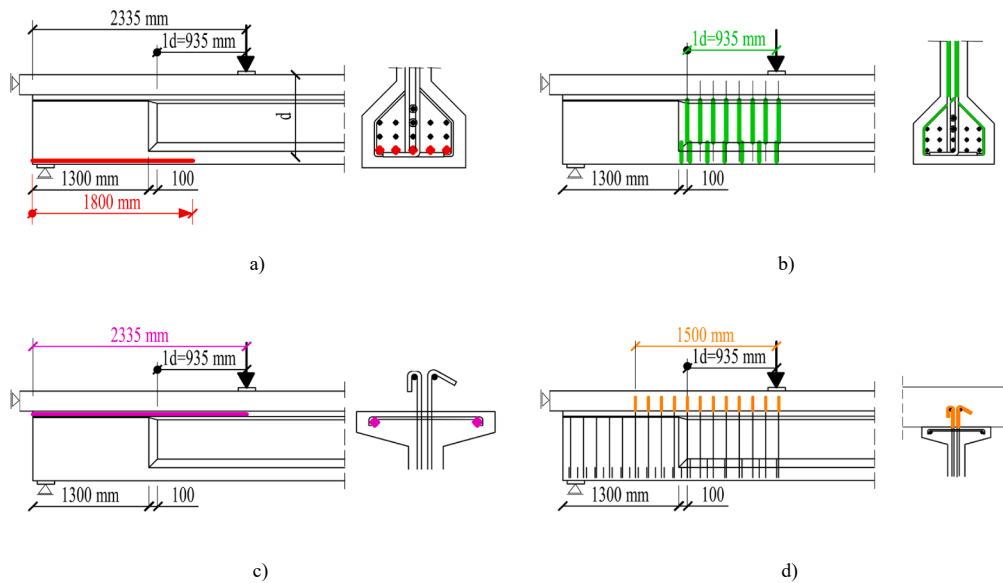

Fig. 6. Corrosion scenarios in individual parts of girder cross-section. a) Corrosion scenario CS1 b) Corrosion scenario CS2 c) Corrosion scenario CS3 d) Corrosion scenario CS4.

Fig. 7. Corrosion in the bottom layer of strands found near the middle support in an NIB girder in Hafrsfjord Bridge near Stavanger.

Table 3
Summary of corrosion scenarios investigated.

Corrosion scenario	Corrosion degree			
	0 %	10 %	20 %	100 %
Uncorroded	P1			
CS1		P1-CS1-18–10	P1-CS1-18–20	
CS2			P1-CS2-20	
CS3				P1-CS3-100
CS4				P1-CS4-100

were assumed in CS1 for all strands in the bottom layer. Although 20 % corrosion may seem a high value, it might still be relevant because significant corrosion of the bottom strands has been observed in NIB girders of bridges in Norway's coastal climate, see Fig. 7. The corrosion length was assumed to be slightly less than the length of the shear span.

The degree of stirrup corrosion in CS2 was assumed equal to 20 %. Corrosion was applied on the vertical parts of the stirrup legs (ø12 and ø6) most exposed to chloride ingress in the web and bottom flange, see Fig. 6b.

Extensive cracking and spalling due to heavy corrosion of the top strands is frequently reported in girder top flanges of pretensioned
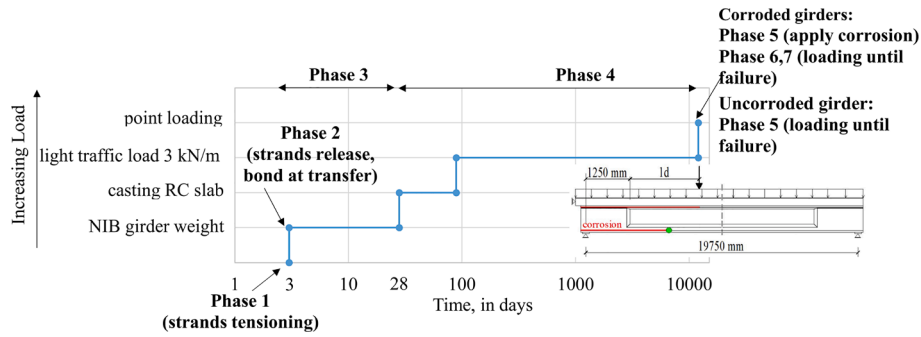
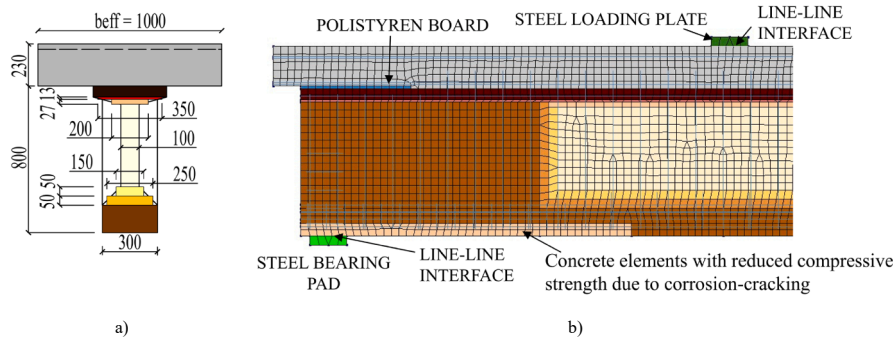**Fig. 8.** Sequence of the NLFE phased analysis.

Fig. 9. FE model a) thickness of the concrete elements, dimensions in mm b) Element subdivision near the middle support.

bridges in Norway [3], so a complete corrosion-induced loss of top strands over the distance from the girder end to the loading point was conservatively assumed in scenario CS3, while complete loss of extended stirrups was assumed in CS4.

An overview of the girders investigated for each corrosion scenario is shown in Table 3.

4.2. Non-linear finite element analysis

To include the main construction phases of the composite NIB girder-slab cross-section as well as time-dependent effects, NLFEAs were performed using the phased analyses approach in Diana 10.5 and a concrete model supplemented with creep and shrinkage functions. The method was proposed in a previous study [50] and modified in this study to take account of corrosion-cracking-induced degradation of concrete properties, modelling the stirrups extended to the plate, more precise modelling of prestress transfer and development length, and improved modelling of the effect of reinforcement corrosion on the prestress degradation. Details of the FE model are given in Section 4.2.1, while the material selections are presented in Sections 4.2.2 and 4.2.3.

The sequence of the phased analysis is shown in Fig. 8. In Phase 1, strands in the bottom and top flanges of the NIB girder were tensioned assuming a very weak bond, while in Phase 2 the strands were released, transferring prestress to the concrete. In Phase 3, the effect on the NIB girder of creep and shrinkage over the first 28 days was included.

Next, it was assumed that, after 28 days of hardening, the NIB girders were transported to the construction site, and the RC slab was cast [43] in Phase 4. We continued calculating the effects of creep and shrinkage on the composite section at regular intervals of time. To include the effect of service loads on the creep and shrinkage effects, the light traffic load was applied on the top of the slab in Phase 4, two months after the RC slab was cast.

After 33 years, the loading up to failure was simulated by applying a 3-point load. The uncorroded girder P1 was loaded in Phase 5. For the

corroded girders, the corrosion was applied instantaneously under sustained loads (self-weight and light traffic load) in Phase 5, prior to the point loading. The corrosion was included in the analyses as a change in 1) the mechanical properties, cross-section area and bond properties of strands (CS1), 2) the cross-section and material properties of stirrups (CS2), and 3) cracked concrete properties (CS1), see details in Section 4.2.3. To account for changes in material properties, the total stresses were recomputed for modified elastic properties. For the assumed complete loss of reinforcement in scenarios CS3 and CS4, the relevant elements were deactivated.

In scenario CS1 with corroded bottom strands, the girders were loaded in Phase 6 until failure of these strands. To simulate broken bottom strands, a 10 mm long piece of each strand (marked in Fig. 8 with the green dot) was removed from the model in Phase 7 and the loading continued until girder failure occurred. In the other corrosion scenarios, the girders were loaded to failure in Phase 6.

4.2.1. Geometry, elements and loading

One NIB girder of full span length and the effective width of the RC slab was modelled with regular plane stress (8-nodes and 6-nodes) and elements with the thickness shown in Fig. 9a. The concrete wear overlay was included in the total height of the RC slab. Regular plane stress elements were also used for modelling the polystyrene board, as well as the loading plate and bearing pads for which a steel material was adopted in this study. In addition, the interaction between the concrete and the steel loading plate and bearing pads was simulated with 2D structural line-line interface elements, see Fig. 9b.

The stirrups and ordinary longitudinal bars were modelled as embedded elements, which implies perfect bond conditions. Each of the strand layers was modelled with truss elements (bond-slip reinforcement type) with a total cross-section and contact perimeter summed from the individual strands in the layer. The third layer of strands from the underside of the girder, see Fig. 3b, was divided into two strand layers, one with the partially debonded strands and one with four fully bonded
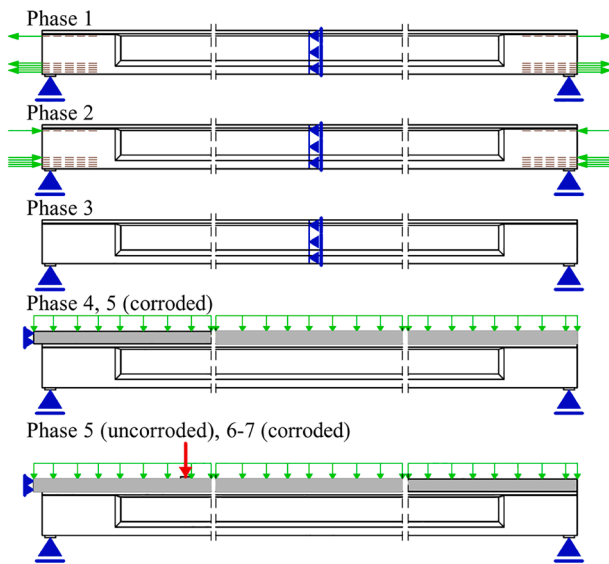
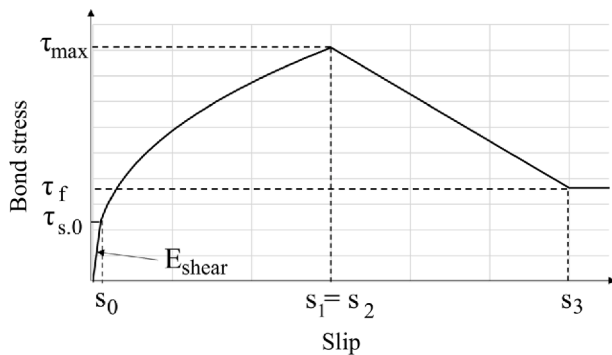**Fig. 10.** Schematic view of supports and loading in analyses phases.

Fig. 11. Schematic view of the bond-slip model for the strands.
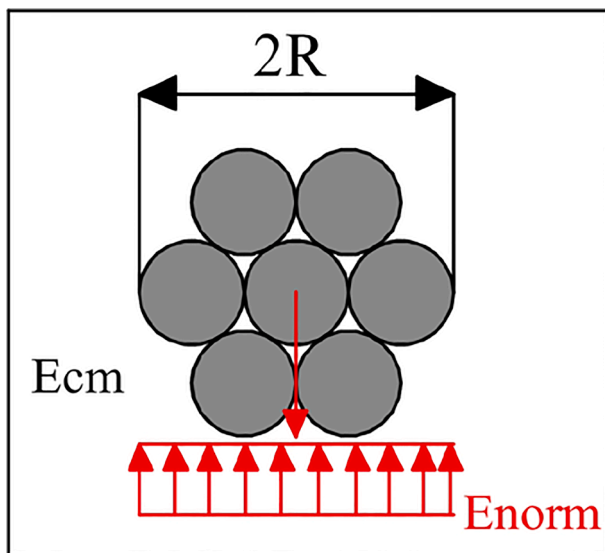

Fig. 12. Schematic view of normal stiffness modulus.

strands. To simulate the bond-slip behaviour of the pretensioned reinforcement, line interface elements for each strand layer were modelled as embedded in the plane stress concrete elements.

In accordance with the analysis phases, the RC slab elements were activated in Phase 4. Fig. 10 shows how the support and loading conditions also changed between the phases. Although only one NIB girder was modelled in this study, the continuity of the slab above the middle support was simulated by restraining the horizontal translation of the slab along its end, see Fig. 10. The self-weight of the NIB girder and RC slab was modelled with factor 1.05, taking account of the embedded reinforcement. In Phase 4, the light traffic load was applied as a uniformly distributed force along the top edge of the slab. Furthermore, the point load was modelled as prescribed displacement applied to the loading plate.

Mesh sensitivity analyses, performed with element sizes of 20 mm, 30 mm and 40 mm on an uncorroded girder, have shown that the girder shear strength was not significantly influenced by the selected mesh size (differences of about 2 %). Consequently, the element size of 40 mm (1/20 of the girder height) was adopted in our analyses to save computational time.

4.2.2. Material modelling of uncorroded girder-slab cross-section

Due to availabilty in Diana, the concrete in the NIB girder and RC slab was modelled using the compression and tension softening curves given in MC2010 [15] and a rotating crack model. The selection of a rotating crack model is supported by a recent comparative study [51]. The models for creep and shrinkage were also chosen from MC2010 [15]. The concrete classes C45 and C25 specified in MC2010 [15] were assumed for modelling the NIB girder and RC slab respectively. This resulted in only 1 N/mm² higher mean compressive strength for the girder than that of the Norwegian concrete originally used. The mean compressive strength modelled for the slab was 3 N/mm² lower than that of the originally used. Moreover, we reduced Young's modulus [15] to 33737 N/mm² and 28808 N/mm² for the NIB girder and RC slab respectively to approximate values given in Table 1. These values are slightly higher than the Young's modulus estimated based on f_{cm} in Table 1. To ensure the required 70 % of 28-day concrete compressive strength in the NIB girder at the time of prestress transfer [46], we assumed a concrete age at loading of 3 days and a rapid hardening cement CEM 42.5R. A normal hardening cement (CEM 42.5 N) and concrete age at loading of 3 h were selected for the RC slab to ensure a realistic low initial stiffness. The notional size of member h was calculated separately for groups of elements with the same thickness and surface exposed to drying. We assumed a concrete age of 5 days at the end of curing (start of drying) for both members, based on common construction practice.

Both strands and ordinary reinforcement were modelled using a simplified elastoplastic material model with strain hardening and material properties given in Table 2. Because no data on the ultimate strains of the uncorroded strands were available, a low conservative value of 4.5 % was assumed based on stress–strain diagrams of a similar steel (1600/1800) widely used in Norway at the time of bridge construction [52].

The debonded parts of the strands were modelled with a cubic bond-slip function, considering a negligible bond strength. The above weak bond model, together with the suppressed superposition of strains and displacement, was also adopted to simulate the no-bond condition during tensioning of the strands in Phase 1 of the analyses.

The bonded strands in the remaining Phases 2–5 were modelled with the bond-slip relationship proposed by Wang et al. [16] and assuming τ_{max} equal to $1.25\sqrt{f_{cm}}$, see Eq. (8) in Section 2.4. Although the concrete at the time of prestress release had not yet reached its design compressive strength, the mean value of the compressive strength at 28 days was assumed for simplicity. The resulting bond strength was about 30 % higher, but sensitivity analyses have shown that the stresses at strand interfaces were still lower than the bond strength calculated for concrete at 3 days after casting. Consequently, the only effect of higher bond strength was that the prestress transfer length decreased by approximately 10 %.

Table 4
Bond-slip properties for uncorroded strands.

$s_1 = s_2$, mm	s_3, mm	α	τ_{max}, N/mm²	τ_f, N/mm²	E_{shear}, N/mm³	E_{norm}, N/mm³
3	12	0.4	9.10	3.64	92.94	2656

To apply the model from Eq. (8) to NLFEA in Diana, the predefined bond-slip model in the fib Model Code 2010 was used, with a relative slip s_1 equal to s_2. Moreover, to define the initial linear shear stiffness E_{shear}, an initial slip s_0 as low as 0.01 mm was assumed, as shown in Fig. 11, and the E_{shear} was applied based on the calculated slope of the bond curve between zero and point s_0, see Eq. (15):

$$E_{shear} = \frac{\tau_{s.0}}{s_0} \tag{15}$$

where $\tau_{s.0}$ is bond stress at initial slip s_0.

To fully define bond characteristics in Diana, it was necessary to apply the linear normal stiffness modulus E_{norm}, which is related to the crushing of the concrete by the strand. The E_{norm} was adopted independently of the bond-slip relationship based on Fig. 12 and Eq. (16) [53]:

$$E_{norm} = \frac{E_{cm}}{2R} \tag{16}$$

where E_{cm} is the Young's modulus of concrete assumed at 28 days, and R is the strand radius. A summary of bond-slip properties is given in Table 4. To validate the applicability of the above model and selected parameters for analyses of pretensioned NIB girders, the resulting prestress transfer length was compared (see Section 5.2) to the values calculated analytically based on national standards.

The steel loading and supporting plates were modelled using an isotropic linear elastic material model with Young's modulus of 200 000 N/mm². Linear elastic material behaviour was also assigned to the Styrofoam board, with Young's modulus of 2000 N/mm² and Poisson's ratio of 0.4. The interface elements between steel plates and concrete

were modelled with a linear elastic material with a normal and shear stiffness of 2400 N/mm³ and 24 N/mm³ respectively, which were calculated in accordance with the Diana FEA guideline [54] based on element size and average Young's modulus of steel and concrete.

Table 5
Material parameters of corrosion-cracked concrete in the bottom flange.

Corrosion degree, %	X, mm	w_{cr}, mm	$f_{cm.cracked}$, N/mm²	$f_{ctm.cracked}$, N/mm²	G_F, N/mm	$E_{cm.cracked}$, N/mm²
10	0.280	3.13	17.15	1.23	0.1218	23,223
20	0.577	6.45	10.00	0.72	0.1105	19,401

- Calculated in this study
- Wang et al. [35],calculated average value for specimens with stirrups
- Wang et al. [35],calculated average value for specimens without stirrups
- Wang et al. [16],calculated average value
- Wang et al. [16],calculated maximum value
- Wang et al. [33],calculated average value
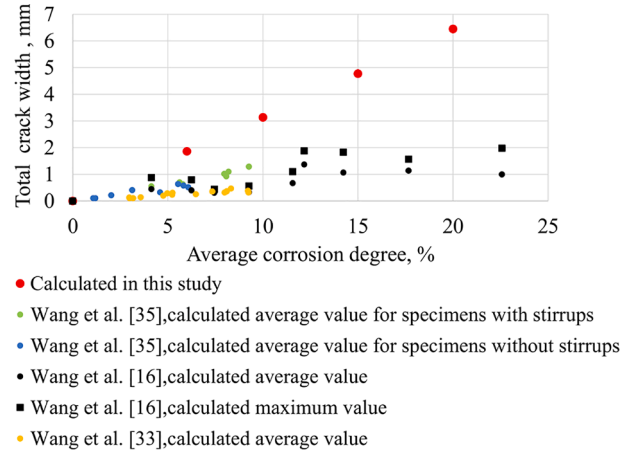
Fig. 14. Total corrosion-induced crack widths in pretensioned elements recorded from experiments.
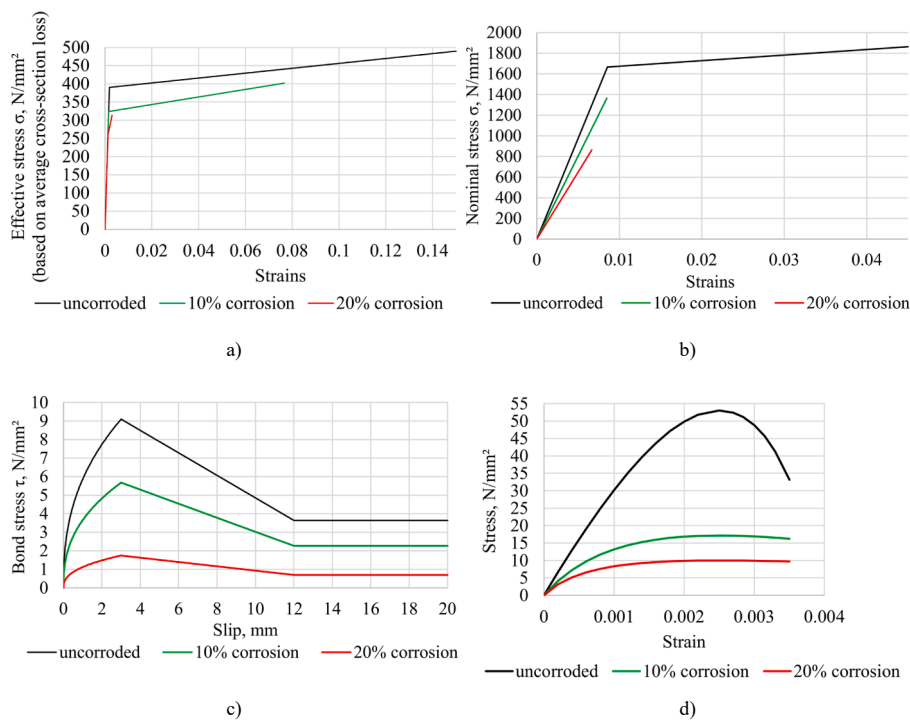

a)

b)

c)

d)

Fig. 13. Constitutive material models for a) reinforcing steel, b) pretensioning strands, c) bond between strands and concrete, and d) concrete in compression.
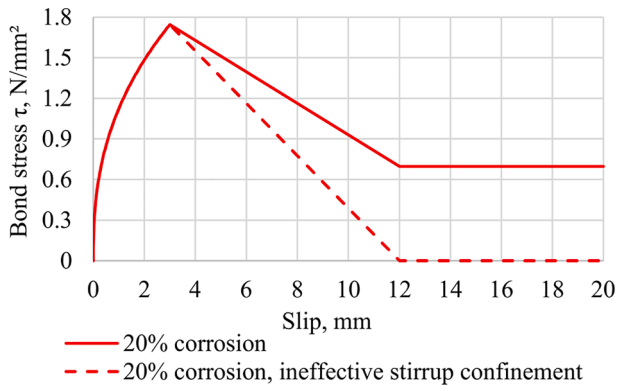
Fig. 15. Bond-slip model for strands with 20% corrosion assuming effective and ineffective stirrup confinement.

4.2.3. Modelling of corrosion

4.2.3.1. Reinforcing steel. Due to lack of experimental tests, the models proposed by Du et al. [18,22] and Cairns et al. [17] were used in this study to reduce the yield strength $f_{y.c}$, ultimate strength $f_{u.c}$ and ductility $\varepsilon_{u.c}$ of corroded stirrups, see Eqs. (1)–(3) in Section 2.2. The maximum values of α_y (0.017) and α_u (0.018) were selected to account for pitting corrosion [17]. The coefficient α_1 was assumed equal to 0.049. The effective stress–strain relationships for corroded and uncorroded ordinary reinforcement are shown in Fig. 13a.

4.2.3.3. Bond between strands and concrete. The bond-slip for corroded strands was modelled using Eq. (8), considering a reduced bond strength based on Eq. (9) in Section 2.4. Accordingly, the bond stiffness was also reduced using Eq. (15). The bond model for varying corrosion levels was closely approximated by the piece-wise linear bond-slip curves shown in Fig. 13c.

4.2.3.4. Concrete. The corrosion-cracked concrete was modelled using the fib Model Code 2010 compression and tension softening curves, for which the effect of corrosion on the concrete compressive strength was estimated based on the model proposed by Coronelli and Gambarova [37], see Eqs. (10) and (11), assuming f_{cm} at 28 days and k equal to 0.1. The crack widths due to corrosion were estimated from Eqs. (12) and (13) assuming v_{rs} equal to 2.78 and equivalent diameters for the uncorroded and corroded strands.

Young's modulus $E_{cm.cracked}$ and fracture energy G_F were derived from MC2010 [15], while the mean tensile strength of the cracked concrete $f_{ctm.cracked}$ was calculated from Eq. (14). The concrete properties for the varying degrees of corrosion are summarized in Table 5.
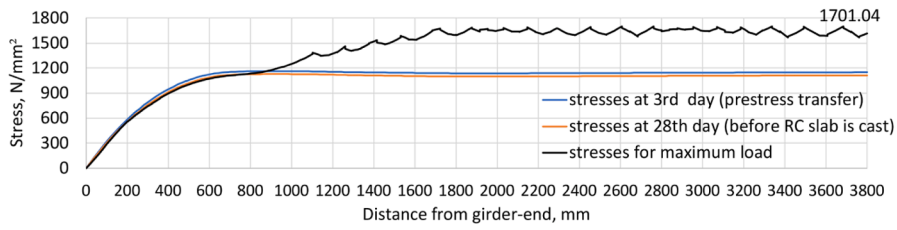
4.2.4. Parametric study

The calculated reductions in compressive and corresponding tensile strength of concrete cracked due to corrosion strongly depend on the number of corroded strands assumed and the crack widths calculated, see Eqs. (10)–(13).
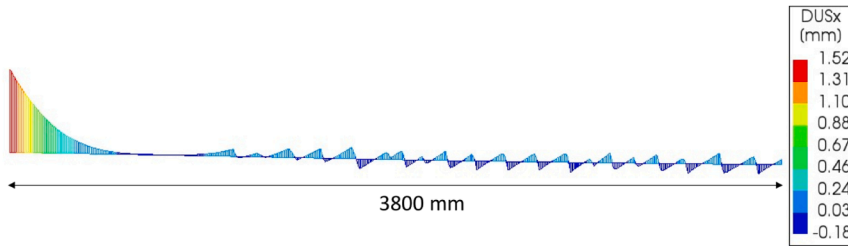
Compared to data in the literature, the crack widths estimated in Table 5 were significantly higher than both average and maximum crack widths found for similar degrees of corrosion in the strands, see Fig. 14.

$$\sigma(\varepsilon) = \begin{cases} E_{s.c}[1 - \rho_s]\varepsilon, \ \varepsilon \leqslant \varepsilon_{py.c} \\ f_{py.c}[1 - \rho_s] + (\varepsilon - \varepsilon_{py.c})\left(\dfrac{f_{pu.c} - f_{py.c}}{\varepsilon_{pu.c} - \varepsilon_{py.c}}\right)[1 - \rho_s], \quad \varepsilon_{py.c} < \varepsilon \leqslant \varepsilon_{pu.c} \\ E_{s.c}[1 - \rho_s]\varepsilon; \varepsilon \leqslant \varepsilon_{pu.c} \qquad \textit{For } \rho_s > 8\% \end{cases} \Bigg\} \textit{For } \rho_s \leqslant 8\% \tag{17}$$

4.2.3.2. Pretensioning strands. For an assumed average corrosion degree, we used the constitutive model proposed by Zeng et al. [28] (see Section 2.3) with further modifications. Since changes in the cross-section of corroded strands between analysis phases are not allowed in Diana, the model from Eq. (4) was modified by multiplying the strength and Young's modulus by the area factor $[1- \rho_s]$ to account for cross-section loss, see Eq. (17):

Moreover, we adopted an effective yield strength $f_{py.c}$ of $0.895f_{pu.c}$ based on the proportions of yield and ultimate strength in uncorroded strands, cf. Table 2. The remaining parameters, $f_{pu.c}$, $E_{s.c}$, and $\varepsilon_{pu.c}$, for corroded strands were calculated from Eqs. (5)–(7).

In the above constitutive model, only the material properties need to be changed in the analyses, and not the cross-section of the strands. The models for corroded and uncorroded strands are shown in Fig. 13b.

The additional analysis P1-CS1-18–20-A with 20 % corrosion in the strands was therefore carried out with an assumed 2 mm crack width, which is a maximum value found in the literature for one strand. The calculated compressive strength, assuming corrosion in all strands of the bottom layer, was about 43 % of the design value. The remaining parameters for the corroded strands and bond, as well as the location of strand fractures, were assumed the same as in P1-CS1-18–20. Since the corrosion-induced crack widths may not correspond to the actual corrosion degree of the strands, and the actual compressive strength of the cracked concrete is unknown, further analysis P1-CS1-18–20-B was carried out with the concrete compressive strength reduced to 30 % of the design value. This enabled us to study the effect of degrading concrete properties on failure mode.
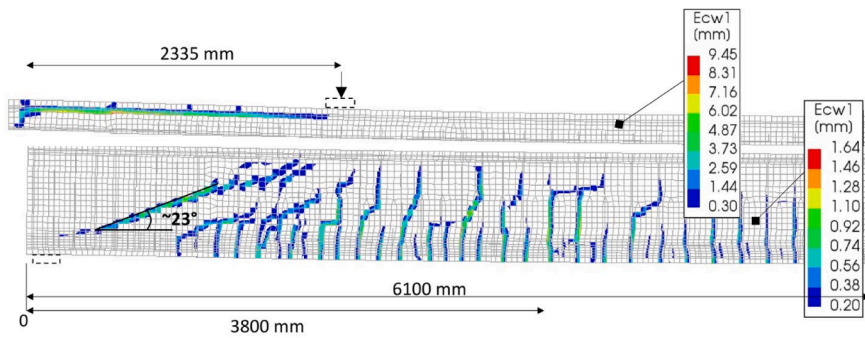
Since stirrups are located nearest the concrete surface and corrode first, the effect of stirrup confinement can be significantly reduced. For the higher strand corrosion level of 20 % in this study, the conservative approach was additionally investigated in P1-CS1-18–20-C by assuming
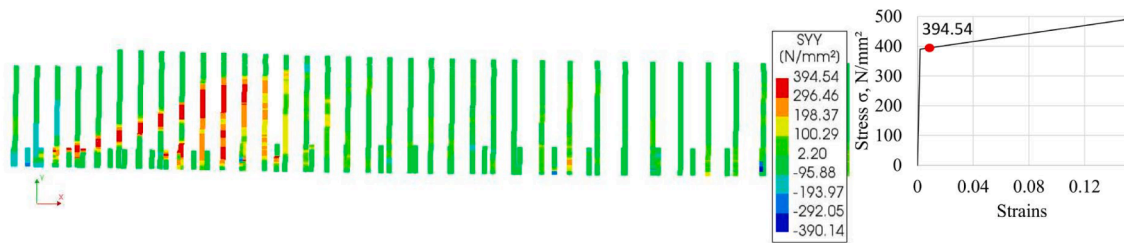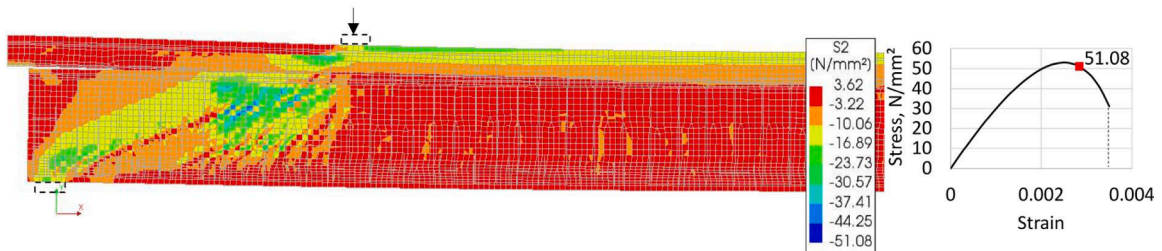
Table 6
Material parameters of corrosion-cracked concrete and residual bond strength for parametric study.

Girder	Concrete properties					Residual bond strength
	w_{cr}, mm	$f_{cm.cracked}$, N/mm^2 (% of design value)	$f_{ctm.cracked}$, N/mm^2	G_F, N/mm	$E_{cm.cracked}$, N/mm^2	τ_f, N/mm^2
P1-CS1-18–20-A	2	22.71 (43 %)	1.63	0.1281	25,502	0.698
P1-CS1-18–20-B	~3.5	15.90 (30 %)	1.14	0.1201	22,643	0.698
P1-CS1-18–20-C	6.45 cf. Table 5	10.00 (19 %)	0.72	0.1105	19,401	0

a)

b)

c)

d)

e)

Fig. 16. NLFEA results obtained for uncorroded NIB girder (P1) near the middle support: a) Evolution of stresses in the bottom layer of strands; b) Slip of the bottom layer of strands for maximum load; c) Crack pattern with crack width in the principal direction for maximum load, shown separately for NIB girder and RC slab; d) Stresses in the stirrups for maximum load; and e) Maximum principal stresses in the concrete for maximum load (Styrofoam board excluded).

Table 7
Shear resistance calculated based on standards.

Shear Resistance V_R, kN	EC2 [48]	NS 3473 [45]
	$\theta = 23°$	$\theta = 45°$
Compressive shear	828[1]	1115
Diagonal tension	1166	732[1][2]

[1] Minimum value

[2] Considering the contribution from the concrete
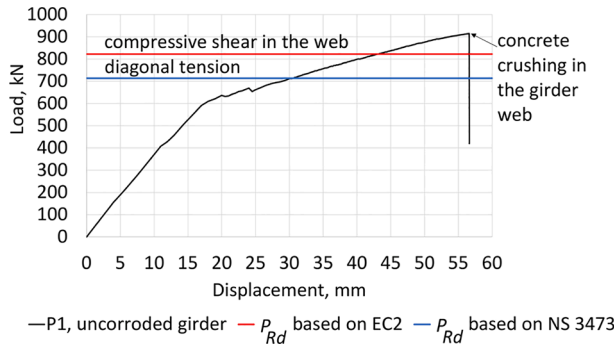
Fig. 17. Comparison of the maximum failure load obtained in NLFEA and load P_{Rd} resulting from shear resistance according to codes and load configuration shown in Fig. 4.

Table 8
Prestress transfer length calculated based on national standards.

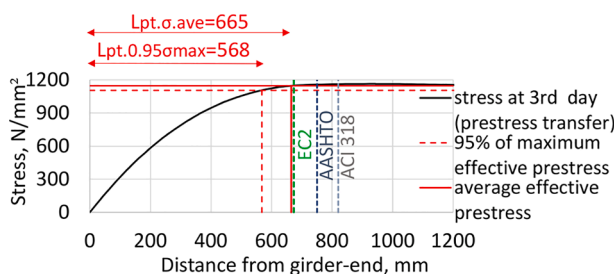| National standard	Model		Calculated prestress transfer length, mm
EC2 [48]	$L_{pt} = \alpha_{p1} \cdot \alpha_{p2} \cdot \varnothing_s \cdot \dfrac{\sigma_{pm0}}{f_{bpt}}$,	(20)	673
	where:		
	$f_{bpt} = \eta_{p1} \cdot \eta_1 \cdot f_{ctd}(t)$,	(21)	
	$f_{ctd}(t) = \alpha_{ct} \cdot 0.7 \dfrac{f_{ctm}(3days)}{\gamma_c}$,	(22)	
	and σ_{pm0} is stress just after releasing equal to 1359 N/mm², $\varnothing_S$ is a strand diameter, α_{p1} equals 1 for gradual release, α_{p2} equals 0.19 and η_{p1} equals 3.2 for 7-wire strands, η_1 equals 1 for good bond conditions, α_{ct} equals 0.85, and γ_C equals 1 for characteristic values of tensile strength at time of release $f_{ctm}(3days) = 2.52N/mm^2$.		
AASHTO [55]	$L_{pt} = 60\varnothing_s$	(23)	750
ACI 318–11 [9]	$L_{pt} = \dfrac{1}{20.7} f_{pe}\varnothing_s$, where $f_{pe} = \sigma_{pm0}$	(24)	820

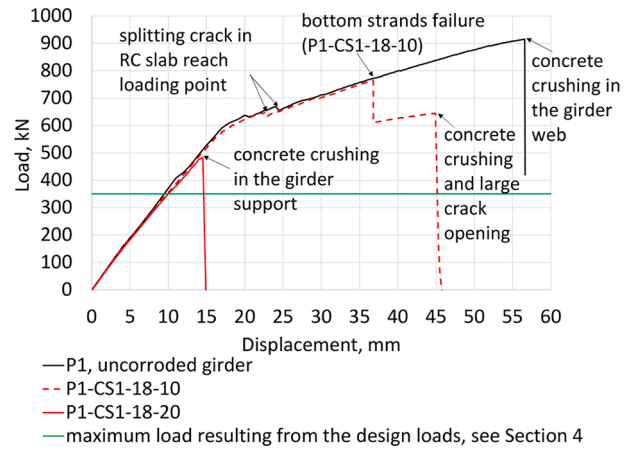**Fig. 18.** Prestress transfer length.

Fig. 19. Load-displacement curves obtained for the uncorroded girder (P1) and the girders with corroded bottom layer of strands (P1-CS1-18).

a residual friction stress τ_f equal to zero to simulate ineffective stirrups. The comparison of bond-slip curves for 20 % corrosion with and without effective stirrup confinement is shown in Fig. 15.

The concrete and bond characteristics studied are summarized in Table 6.

5. Numerical results

5.1. Uncorroded girder

The results described in this section clearly illustrate the diversity of the failure development in the structural system investigated. The development of stresses in the bottom layer of the strands, from prestress transfer to maximum load, is shown in Fig. 16a. As expected, the stresses decrease over the first 28 days due to concrete creep and shrinkage, but later increase due to loading and cracking.

At maximum load just before failure, the stresses in the strands exceed the yield strength, cf. Table 2, while Fig. 16b shows that no cracks or excessive strand slippage affect the prestress transfer length.

The first cracking occurs as vertical cracks in the slab near its support, i.e., in the continuity area above the middle support, and it evolves into a rather long horizontal splitting crack along the top reinforcement in the slab, as shown in Fig. 16c. While the splitting crack propagates towards the loading point, a horizontal crack starts to appear in the transition zone between the girder web and the top flange, followed by diagonal shear cracking in the web. With further load increase, 1) flexural cracks appear, 2) the splitting crack in the slab reaches the loading point, and 3) a major shear crack propagates towards the support with an angle of about 23°. Consequently, extensive cracking due to both flexure and shear is present before failure occurs, see Fig. 16c.

The large splitting crack in the top of the slab can be explained by large shear stresses and the fact that the vertical stirrups do not reach the level of the top reinforcement, cf. the reinforcement layout presented in Fig. 3.

The stresses in the stirrups in the girder reached yielding before the maximum load level as shown in Fig. 16d. Furthermore, the compressive strength was reached in both the slab (next to loading plate) and in the girder web, see Fig. 16e. Although yielding occurred in all reinforcement types and the stirrups in particular are a long way from tensile failure, the failure mode is governed by concrete crushing in the struts in the girder web and in lower parts of the slab, see Fig. 16e.

5.2. Validation with analytical calculations and regulations
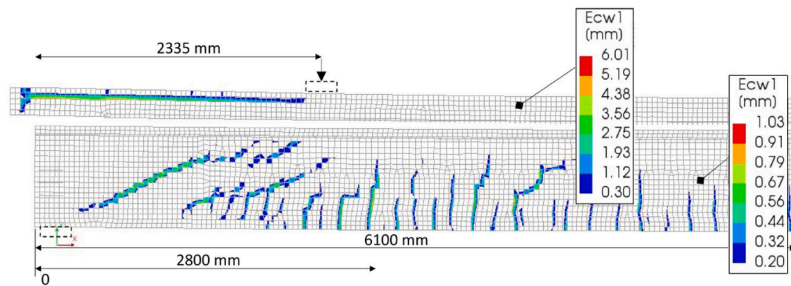
To calculate the shear resistance V_R of the uncorroded girder with RC slab according to EC2 [48], the inclination of main concrete compressive
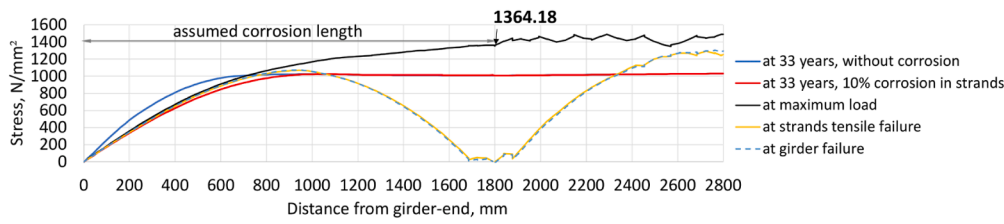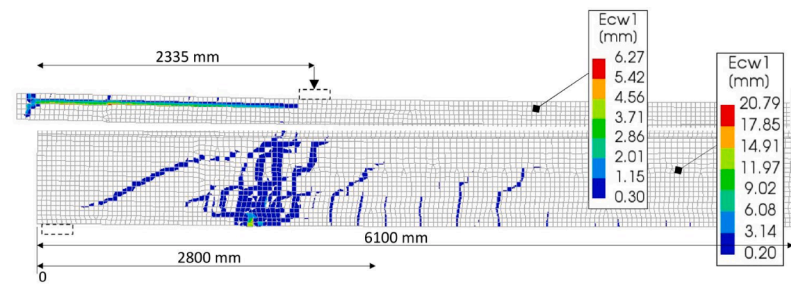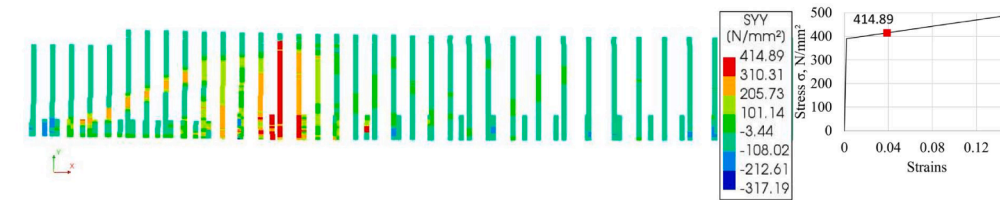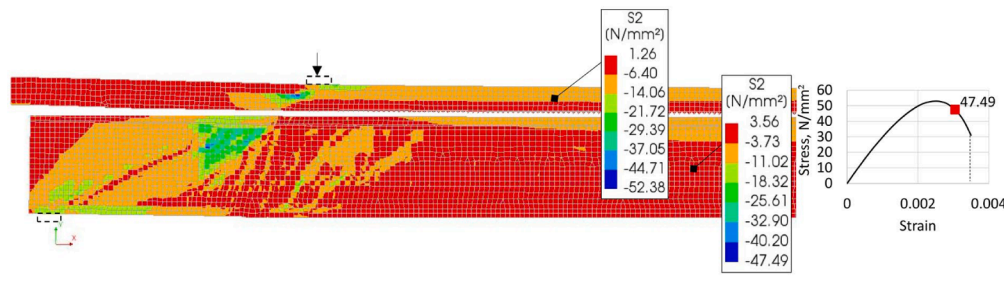
a)
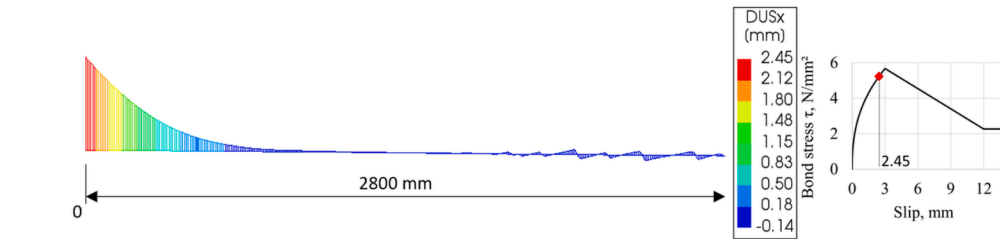
b)

c)

d)

e)

f)

Fig. 20. NLFEA results obtained near the middle support for P1-CS1-18–10: a) Evolution of stresses in the bottom layer of strands; b) Slip in the bottom strand layer at maximum load; c) Crack pattern with crack width in the principal direction at maximum load, shown separately for NIB girder and RC slab; d) Crack pattern with crack width in the principal direction at girder failure, shown separately for NIB girder and RC slab; e) Stresses in the stirrups at girder failure; and f) Maximum principal stresses in the concrete at girder failure (Styrofoam board excluded), shown separately for NIB girder and RC slab.
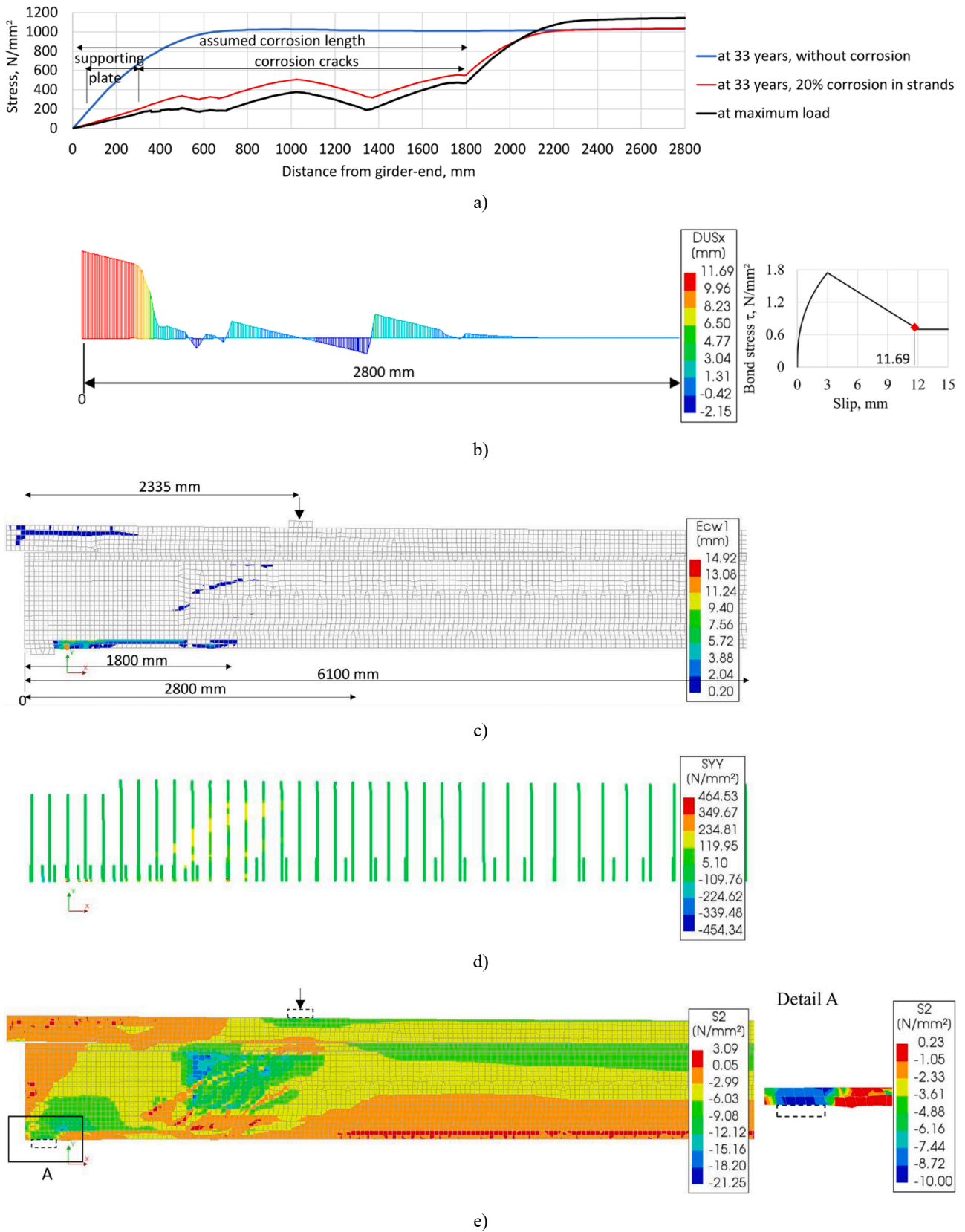
Fig. 21. NLFEA results obtained near the middle support for P1-CS1-18–20: a) Evolution of stresses in the bottom layer of strands; b) Slip of the bottom strand layer at maximum load; c) Crack pattern with crack width in the principal direction at maximum load; d) Stresses in the stirrups at maximum load; and e) Maximum principal stresses in the concrete at maximum load (Styrofoam board excluded).
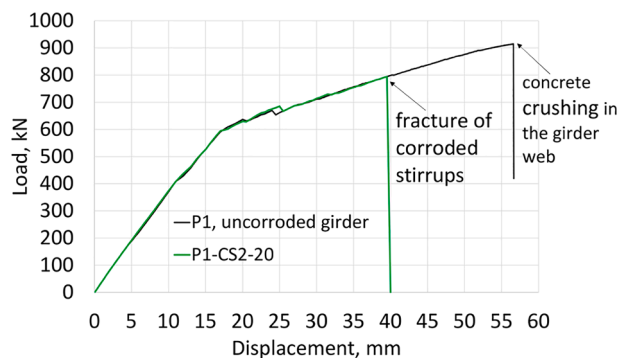
Fig. 22. The load–displacement curves obtained for the uncorroded girder (P1) and the girder with corroded stirrups (P1-CS2-20).

strut θ was assumed to be 23°, equal to the angle of main shear crack shown in Fig. 16c. This angle is between the limiting values of 21.8° and 45° recommended by the standard [48]. To calculate the V_R according to NS 3473 [45], the recommended θ of 45° was used. The shear resistance V_R values obtained are listed in Table 7. Next, the minimum values of V_R were used to express the shear resistance in terms of applied loads P_{Rd} as explained in Section 4, and P_{Rd} values were compared in Fig. 17 to the maximum failure load obtained in NLFEA.

As expected, the load P_{Rd} predicted using a shear resistance based on EC2 [48] was lower than the maximum failure load obtained in NLFEA. Nevertheless, the difference was only about 10 %, and the type of failure obtained in both NLFEA and analytical predictions were the same. The load P_{Rd} predicted based on NS 3473 [45] was about 22 % lower than the maximum failure load obtained in NLFEA. The larger difference is related to the larger inclination θ assumed, which causes greater utilization of stirrups. Nevertheless, it can be concluded that the difference between the capacity of the girder obtained in NLFEA and analytical calculation, particularly based on EC2 [48], is acceptable.

In addition, the prestress transfer length was compared to values calculated in Table 8 based on EC2 [48] and the American standards AASTHO (2012) [55] and ACI 318 [9]. The simulated prestress transfer length was considered as the distance to a point with 95 % of the maximum effective prestress [56] or the average effective prestress in the strands. Both transfer lengths obtained were shorter than the design values, see Fig. 18. This may be due to the actual strand circumference or a higher bond strength (at 28th day) used in NLFEA. Nevertheless, the difference is rather low, especially in relation to the transfer length based on EC2 [48]. The model proposed by Wang et al. [16] was developed for strand pull-out, but it can also be used for modelling push-in of the strands during prestress release with sufficient accuracy.

5.3. Corrosion scenario CS1

Fig. 19 shows the load–deflection relationship for the uncorroded beam in corrosion scenario CS1 with 10 % and 20 % corrosion along the strands. Corrosion in the bottom layer of strands near the support reduced the girder capacity by about 16 % and 47 % for the two levels of corrosion and also greatly reduced the ductility of the girder. Moreover, the failure mode changed from concrete crushing in the girder web to tensile failure in the strands combined with concrete crushing and large crack openings with 10 % corrosion, and brittle failure caused by concrete crushing above the support with 20 % corrosion. In both cases, however, the girder capacity was greater than the maximum load resulting from the design loads, as explained in Section 4 and Fig. 5. This may be due to the high safety margin of the girders analysed, which may result from the standardization of their geometry and the reinforcement layout, i.e., the lack of individual optimization.

The degradation in bond for strands with 10 % corrosion (P1-CS1-18–10) resulted in reduced prestress near the support and a

corresponding increase in the prestress development length of about 28 % as shown in Fig. 20a. Subsequent loading increased stress in the strands until the ultimate strength of 1363 N/mm^2 was reached in the corroded part of the strands. After tensile failure in the strands, redevelopment of the prestress occurred, see Fig. 20a, but the second and third layer of bonded strands then yielded immediately, and the overall capacity was not restored.

The strand slip at maximum load increased by only 0.9 mm compared to the uncorroded case, cf. Figs. 20b and 16b. Moreover, extensive flexural and shear cracking were present at the maximum load as in the uncorroded case, see Fig. 20c. Subsequent loading caused considerable flexural cracking in the area surrounding broken strands, see Fig. 20d, leading to failure of the girder. Fig. 20e shows how the stirrups yielded at failure but did not reach failure. At the same time, the concrete stresses in the struts in the girder web exceeded the compressive strength, and the concrete crushed in the slab near the loading plate, see Fig. 20f. The overall failure mode was complex and due to strand fractures followed by large crack widths and concrete crushing in the girder web and slab.

Fig. 21 gives detailed results for the scenario with 20 % corrosion in the bottom strands (P1-CS1-18–20). The reduction in the tensile strength of the concrete surrounding the corroded strands resulted in longitudinal corrosion cracks just beyond the supporting plate over a distance of 1550 mm. The corrosion cracking and the significant reduction in bond strength due to corrosion considerably reduced the prestress over the corroded length, see Fig. 21a. The prestress further redevelops in the remaining uncorroded part of the strands.

The large strand slip of 9.24 mm occurred due to the degradation of bond and concrete strengths. With further loading, the slip increased to 11.69 mm, close to bond-slip failure, see Fig. 21b. The cracking behaviour at maximum load just before failure also differed from the uncorroded situation. After the corrosion-induced cracking appeared along parts of the bottom strands, the splitting crack in the slab propagated, and in this scenario just one major shear crack opened in the girder web, as shown in Fig. 21c. Due to the small width of the shear crack, the stirrups yielded only in the location of the corrosion crack at the bottom of the girder, see Fig. 21d. A major effect of this, however, is that the corrosion crack above the support drastically reduced the compressive strength in this area to 10 N/mm^2, cf. Fig. 21e. Consequently, the failure occurred due to concrete crushing in the support area, a result which explains the low ductility observed in Fig. 19.

5.4. Corrosion scenario CS2

Fig. 22 shows the load–deflection curves for corrosion scenario CS2 and the uncorroded girder. 20 % corrosion in the stirrups of the girder web does not reduce the stiffness of the girder, but the failure mode changes from concrete crushing in the web to fracture of the stirrups with about 13 % less load. 20 % stirrup corrosion was found to have less influence on the girder capacity than 20 % corrosion in the bottom strands, cf. Fig. 22 and Fig. 19.

The distribution of stress and slip along the strands at maximum load does not differ from the uncorroded girder, except that the maximum prestress is about 10 % lower. These results are therefore not repeated in this section. Moreover, extensive flexural and shear cracking occurs prior to failure just as in the uncorroded case, see Fig. 23a. Corroded stirrups, however, reach ultimate stresses (313 N/mm^2) and strains (0.003) before the concrete compressive strength is reached in the struts of the web, as shown in Fig. 23b and c. Consequently, failure occurs due to stirrup fracture in the girder web.

5.5. Corrosion scenarios CS3 and CS4

Considerable corrosion in the top strands (P1-CS3-100) or in the extended stirrups near the support (P1-CS4-100) affects neither the capacity of the NIB girder nor its failure mode, see Fig. 24. The partial loss
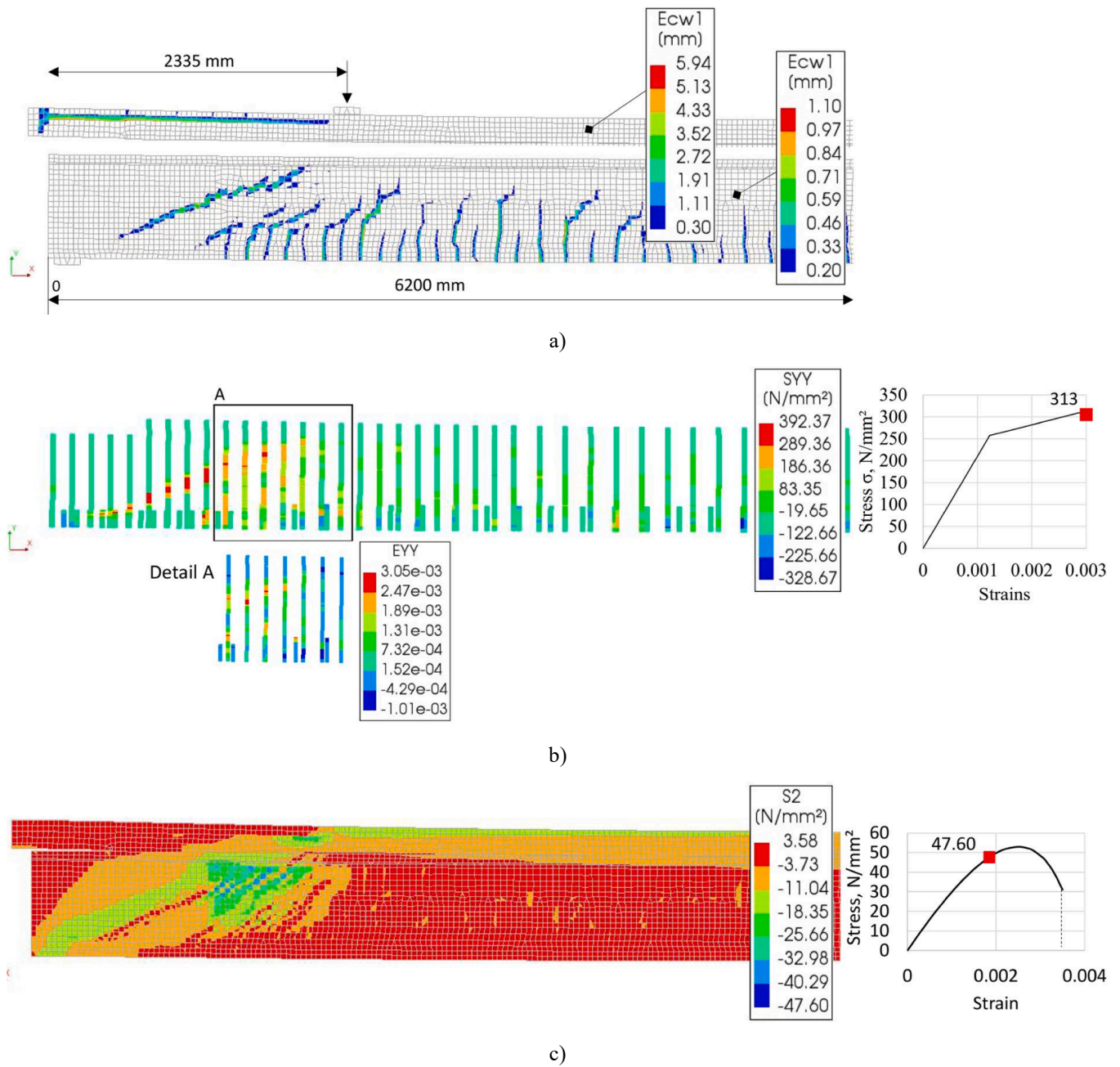
Fig. 23. NLFEA results obtained near the middle support for P1-CS2-20: a) Crack pattern with crack width in the principal direction at maximum load; b) Stresses and strains in the stirrups at maximum load; and c) Maximum principal stresses in the concrete at maximum load (Styrofoam board excluded).

of top strands caused only minor change in the tensile stresses of the bottom strands and a redistribution of stressess in concrete within the shear span, which did not affect the girder behaviour for higher loads. The loss of extended stirrups had almost no impact on the stressess in the remaining part of the stirrups or the RC slab, which implies their lack of contribution to girder performance.

5.6. Results of parametric study

Fig. 25 shows the load–displacement curves for the uncorroded girder and the girder with 20 % corrosion in the strands and varying concrete and bond parameters, as explained in Section 4.2.4. In contrast to the previously described case with 20 % corrosion and concrete strengths reduced to 19 % of the design value near the middle support, the girders with strengths reduced to 30 % and 43 % (P1-CS1-18-20A/B)

failed at higher loads and due to large crack widths combined with concrete crushing in the slab.

Once ineffective stirrup confinement was assumed for the case with 20 % corrosion in the strands and the highest reduction in concrete compressive and tensile strength was 19 % of the design value, the girders failed due to strand slippage (P1-CS1-18-20C). The capacity and ductility in this case were only 45 % and 21 % of the corresponding values for the uncorroded girder, and only slightly higher than the maximum load resulting from design loads.

The structural behaviour of girders P1-CS1-18-20A and B are similar. Detailed results are therefore shown only for the girder with slightly lower capacity (Girder 20B). Fig. 26a shows that the bottom layer of the strands fractured at the assumed location (1.8 m from girder end) immediately after applying 20 % corrosion. Consequently, the girder stiffness was reduced as shown previously in Fig. 25. Despite the fracture
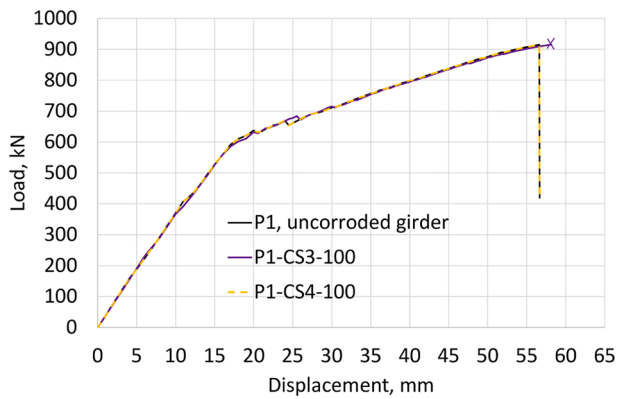
Fig. 24. Load-displacement curves obtained for the uncorroded girder (P1), the girders with corroded top strands (P1-CS3-100), and the girders with corrosion in the extended stirrups (P1-CS4-100).
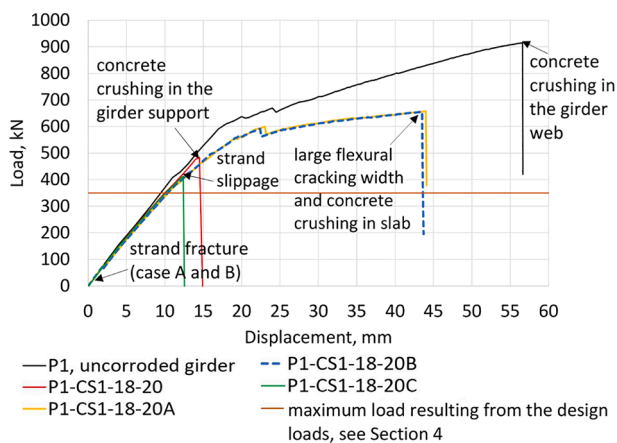

Fig. 25. Load-displacement curves obtained for the uncorroded girder (P1) and the girders with 20% corrosion in the bottom layer of strands assuming varying concrete or bond parameters as described in Table 6.

of the strands, the load could subsequently be increased. It should be noted that the ultimate strength of 863 N/mm^2 in the corroded strands had already been reached about 1.3 m from the girder end. Nevertheless, the assumed fracture location can be justified by the uneven corrosion distribution in real structures and the highest local reduction of the strand cross-section being at a greater distance.

The 5 mm slip in the bottom strands, shown in Fig. 26b for maximum load, may be noticeable but did not cause the anchorage failure. The flexure and shear cracking, however, were extensive, with the pattern similar to the case with 10 % corrosion, compare Fig. 26c with Fig. 20d. The stirrups also yielded but did not fracture, as shown in Fig. 26d, and the concrete compressive stresses in the girder did not exceed the compressive strength, see Fig. 26e. Failure therefore occurred due to large crack widths reaching the zone of crushed concrete in the slab.

In case P1-CS1-18-20C, the reduced descending part of the bond-slip curve, shown in Fig. 15 for corroded strands with ineffective stirrups, resulted in significant instant slippage of 11.38 mm, larger than in case P1-CS1-18–20. Subsequent loading increased the slip to more than 12 mm, see Fig. 27, and anchorage failure occurred. The crack pattern at failure was similar to the case P1-CS1-18–20 shown in Fig. 21c.

6. Discussion

The numerical study shows that only the corrosion of the bottom strands and stirrups modified the failure mode of the girders analysed. Corrosion of the stirrups extended to the plate did not affect the

composite action between girder and slab, or therefore the girder performance. Except that those stirrups do not confine the top layer of slab reinforcement in the shear-critical sections, the reason might be the perfect bond assumed in NLFEA between slab and girder. Although the bond quality may be overestimated, the rough top surface of the pretensioned girders was required when casting [57], which means sufficient bonding to the cast-in-place slabs can be expected.

The NLFEA of the girder with corroded top strands does not assume any reduction of concrete properties due to corrosion cracking. This simplification can be justified with the presence of only two strands shown in the Fig. 3a, corrosion of which would cause spalling of the flange corners rather than cracking across the whole width of the top flange. Given the severe corrosion, the reduction in the concrete compressive strength calculated using Eqs. (10)–(13) can be unrealistically high. The effect of the reduced width of the top flange on the shear strength of the girder-slab interface can be studied with more realistic 3D modelling. Nevertheless, it is unlikely that corrosion in the top strands would cause failure of the girder in normal load conditions, assuming composite action in the remaining (non-spalled) area of the girder-slab joint.

In the girders with moderate 10 % corrosion of the bottom layer of strands near the support, the fracture of corroded strands occurs without significant strand slippage. This agrees with the study by Wang et al. [33], which found that for strand corrosion greater than 6.5 % the effect of the tensile strength deterioration on the failure mode and capacity of the pretensioned beams was more significant than the deterioration of the bond. However, for strand corrosion as high as 20 % in this study, we obtained not only strand fracture but also strand slip or concrete crushing in the support. The numerical prediction of the failure mode strongly depends not only on the degradation models for mechanical properties and the bond of the strands, but also on the properties of corrosion-cracked concrete.

Reduction in concrete compressive and tensile strength of as much as 70 % of the design value significantly reduced the prestress and increased the development length in the bottom layer of strands but did not cause the concrete to crack along the corroded length, see Fig. 28. A reduction of 81 % in the concrete strengths was required in the FE analyses to introduce corrosion splitting cracks. As Fig. 28 shows, this cracking reduces the prestress to a value significantly lower than tensile strength, which inhibits strand breakage.

However, such a large reduction in compressive strength was calculated based on the model for crack width developed for the rebar. The various geometrical properties of the strand may result in both different corrosion penetration depths and increases in its volume due to the expanding corrosion product. For instance, at 20 % corrosion, the penetration depth calculated in this study for a bar with a cross-section equivalent to the strand is higher than the penetration depth estimated for an actual strand shape when only corrosion on the outer wires is assumed, see Fig. 29. Considering that the summarized crack width is equal to the increase in the external perimeter of corrosion product [37,40], Eq. (26) presented in another study [42] could be used for calculating crack width for an actual strand shape. However, the formula given below yields a crack width of 18.6 mm, about 3 times greater than that based on the Molina et al. model [40], cf. Table 5.

$$w_{cr} = \Sigma u_{i.corr} = 6 \cdot \left(\frac{2}{3} \cdot 2\pi(\nu_{rs} - 1)\chi \right) = 8\pi(\nu_{rs} - 1)\chi \qquad (26)$$

It should be noted that the Molina et al. model [40] does not include the effect of filling the pores and cracks with rust, nor the influence of concrete cover thickness, which can generate a modelling error [58]. In addition, the crack width prediction is not only sensitive to the ratio of volumetric expansion of corrosion product, which may vary from the assumed average value, but also to the compressive stresses generated in the concrete by prestress [41]. The calculated crack widths based on a stress-free state [40] therefore differ from the width numerically
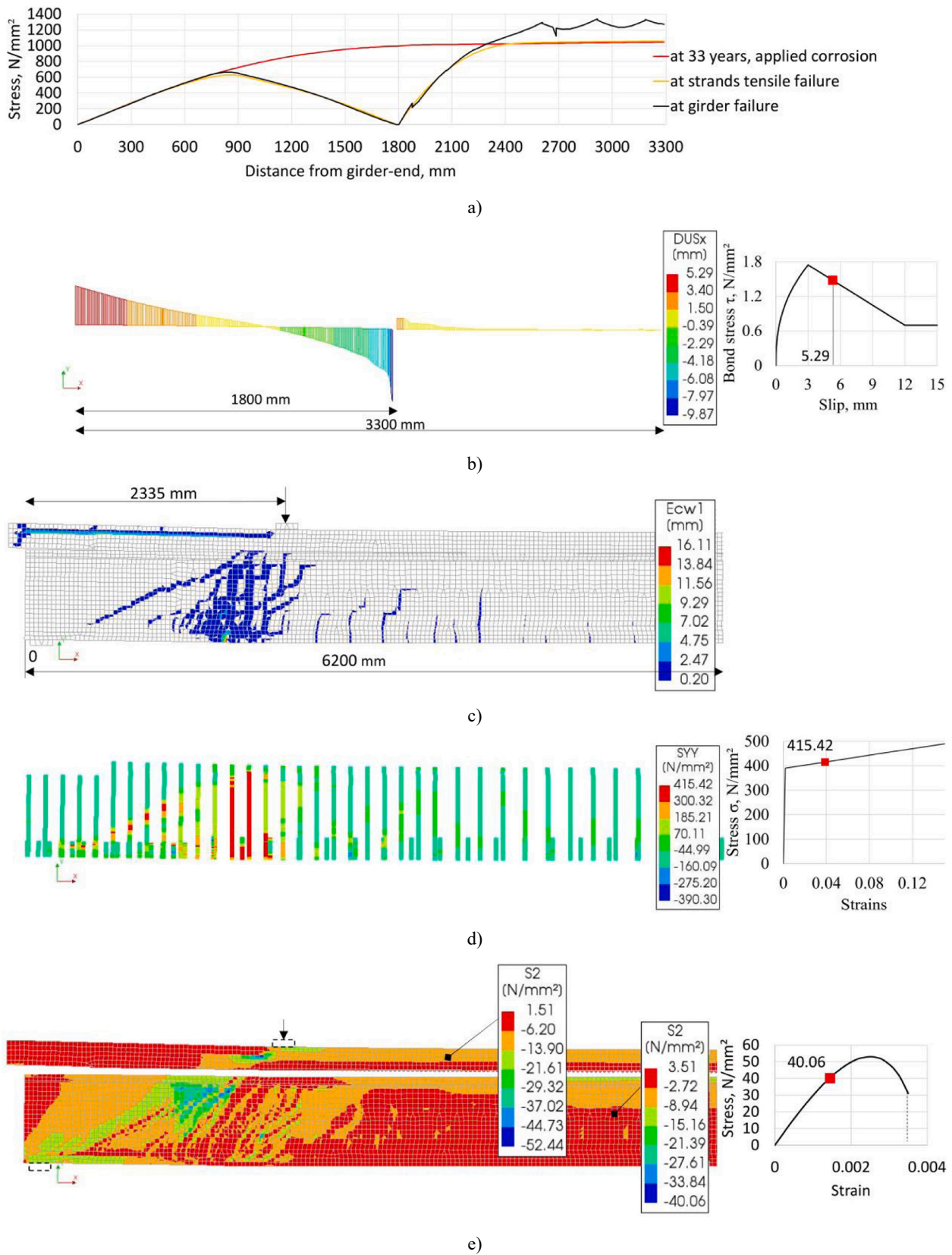
a)

b)

c)

d)

e)

Fig. 26. NLFEA results obtained for P1-CS1-18-20B near the middle support: a) Evolution of stresses in the bottom layer of strands; b) Slip of the bottom strand layer at maximum load; c) Crack pattern with crack width in the principal direction at maximum load, with NIB girder and RC slab shown separately; d) Stresses in the stirrups at maximum load; and e) Maximum principal stresses in the concrete at maximum load (Styrofoam board excluded), shown separately for NIB girder and RC slab.
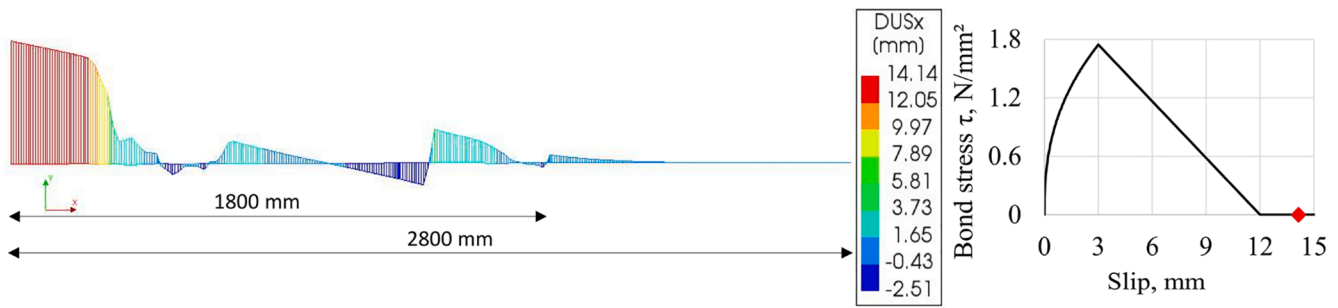
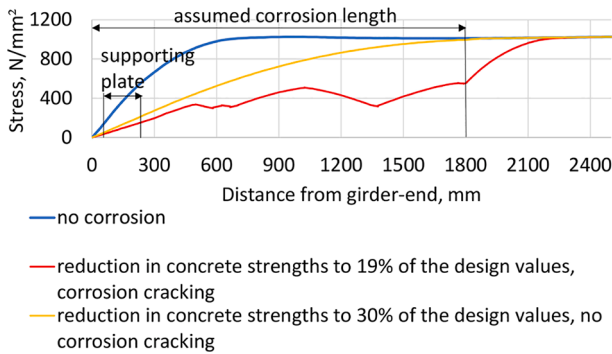**Fig. 27.** Slip of the bottom strands layer for maximum load obtained for P1-CS1-18-20C near the middle support.

Fig. 28. Difference in prestress distribution between corrosion cracked and uncracked concrete.
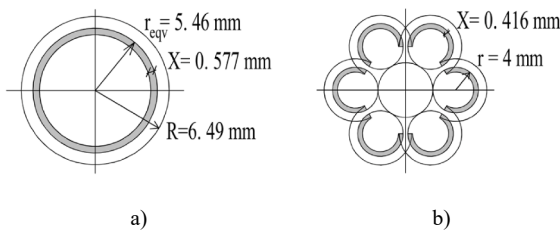

Fig. 29. Calculated penetration depth for 20% corrosion assuming a) rebar shape with a cross section equivalent to the strand, and b) strand shape.

obtained in the anchorage zone, where prestress gradually increases with the distance from the girder end. Finally, for structures exposed to chlorides, pitting corrosion was typically observed instead of an

assumed uniform corrosion. The distribution of pitting corrosion across and along the corroded length also affects its cracking and its modelling reliability [58,59].

Considering the above factors, the calculation of crack widths requires more studies and validations against experimental data. Nevertheless, for strand corrosion levels as high as 20 %, the corrosion of the stirrups and mounting bars located close to the concrete surface is even more severe and can lead to concrete cover cracking and delamination. Such extensive cracking has been reported near supports of pretensioned NIB girders in Norway, see Fig. 30. Severe cover cracking has also been found for only small corrosion spots on the strands but severe and moderate corrosion of the mounting bars and stirrups respectively [6]. This implies that the assumption of very low compressive strengths of cracked concrete cover near supports may be realistic.

The development of cracking in the case with failure in the anchorage zone may show some similarity to the cracks observed in the field, particularly those propagating from the top of the web for a load lower than the maximum load of 350 kN estimated in Section 4 from the design loads, cf. Fig. 31 and Fig. 1c. Those types of crack, however, also
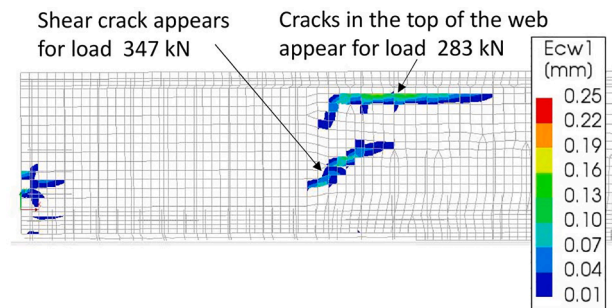

Fig. 31. Crack development in the girder for P1-CS1-18–20 and P1-CS1-18-20C.

Fig. 30. Corrosion cracking in bottom of pretensioned girders: a) significant corrosion cracking in the NIB girder bottom flange near support, bridge close to Kristiansund; and b) corrosion cracking and spalling in the NIB girder-ends, photo by NPRA [7].

appear for similar load levels in the uncorroded girder and the girder with lower corrosion levels in the strands. The load needed for the appearance of the shear crack shown in Fig. 31 is comparable to the maximum load resulting from the design loads. However, it should be noted that the maximum load obtained in the support is higher than the point load applied at the section checked. This means that some overloading is nevertheless expected which will actually initiate the predicted shear crack.

The predicted failure load for the worst scenario is only about 1.2 times higher than the maximum load resulting from typical traffic loads. Although girder failure is not expected until overloading occurs, pretensioned girders that have severe corrosion cracking in the bottom flange near the support should be monitored closely for the presence of shear cracks and strand slip, which can be measured if the girder end surface is exposed. In cases without significant corrosion cracking in the bottom flange, the warning signs of flexural and shear cracks would appear before failure, which agrees with another study [60] on girders with moderately corroded strands in girder ends.

7. Conclusions and suggestions for further work

The non-linear finite element study was performed on the pretensioned bridge girders with RC slabs to investigate the effects on their capacity and failure mode of corrosion damage typically observed near supports. Based on the real case study of Dalselv Bridge girders, we investigated the effect of the level of corrosion and its location (bottom flange, top flange, web and girder-slab interface). The numerical approach considers construction phases and time effects such as concrete creep and shrinkage, as well as corrosion-induced reduction in reinforcement cross-section and degradation in the material properties of the steel, concrete and bond of the strands. Also, the influence of modelled parameters of cracked concrete and bond was investigated. From the results of non-linear finite element analysis of uncorroded and corroded pretensioned girders, the following conclusions can be drawn:

1. At high loads, extensive flexural and shear cracking occurs in uncorroded girders, which fail due to concrete crushing in the girder web. The capacity is sufficient, and clear warning signs will occur before possible failures. Moreover, the capacity of such a girder obtained from NLFEA in this research was comparable to analytical calculation based on EC2.
2. Moderate (10 %) corrosion of the bottom strands near supports modifies the failure mode of pretensioned girders from concrete crushing in the girder web to tensile failure of the strands. Prior to strand fracture, extensive flexural and shear cracking occurs as in uncorroded girders, and the ductility is only slightly reduced.
3. Large (20 %) corrosion of the bottom strands together with corrosion of confining stirrups and mounting bars may induce severe cracking in the girder bottom flange and cause brittle failure due to strand slippage or concrete crushing in the support with minimal shear cracking.
4. In all cases investigated, the predicted shear capacities were higher than the maximum load resulting from typical design traffic loads. Some similarities were noticed between crack patterns predicted in NLFEA and observed in field, but girder failure is not expected until overloading occurs.
5. Prediction of the shear performance of corroded girders strongly depends on the material models and parameters selected, especially concrete compressive and tensile strength reduced due to corrosion cracking. The calculation of crack widths in particular requires more research and validation with the data from the field, especially for combined corrosion of strands, confining stirrups and mounting bars.
6. Corrosion in the top strands and stirrups extended to the RC slab does not degrade girder capacity. Repairs of the top girder flange can be carried out, but such damage does not threaten girder failure.

Since this study assumed only one shear span-to-depth ratio and equal corrosion in all strands in the bottom layer, the performance of corroded pretensioned girders should also be studied with larger shear spans or corrosion varying between strands. It is also recommended to investigate the combined effect of higher degrees of corrosion in strands and stirrups. In addition, tensile tests of the strands used at the time of construction would provide more information on their actual ductility. Finally, shear tests on decommissioned bridge girders would provide valuable validation of numerical studies in the future.

It is also recommended tomonitore closely pretensioned bridge girders with severe cracking in their bottom flanges near supports, especially when shear cracking appears. For girders with exposed end surfaces, the strand slip can be measured as an indicator of potential anchorage failure. The ultimate goal of the research is to arrive at validated probabilistic life predictions [61].

Declaration of Competing Interest

The authors declare that they have no known competing financial interests or personal relationships that could have appeared to influence the work reported in this paper.

References

[1] Bruce SM, McCarten PS, Freitag SA, Hasson LM. Deterioration of prestressed concrete bridge beams. Land Transport New Zealand Research Report 337; Wellington, 2008.

[2] Pough K, Mayhorn D, Prinz GS, Floyd RW. Evaluation and repair of existing bridges in extreme environments. University of Oklahoma. School of Civil Engineering and Environmental Science; 2016.

[3] Osmolska MJ, Kanstad T, Hendriks MAN, Hornbostel K, Markeset G. Durability of pretensioned concrete girders in coastal climate bridges: Basis for better maintenance and future design. Struct Concr 2019;20(6):2256–71. https://doi.org/10.1002/suco.201900144.

[4] Takeda K, Tanaka Y, Shimomura T, Yamaguchi T, Kuga S, Ibayashi K, et al. Loading test and numerical evaluation of the residual strength of pre-tensioned PC beam affected by chloride attack [in Japanese]. J Japan Soc Civ Eng Ser E2 (Mater Concr Struct) 2015;71(4):303–22. https://doi.org/10.2208/jscejmcs.71.303.

[5] Belletti B, Vecchi F, Bandini C, Andrade C, Montero JS. Numerical evaluation of the corrosion effects in prestressed concrete beams without shear reinforcement. Struct Concr 2020;21(5):1794–809. https://doi.org/10.1002/suco.201900283.

[6] Osmolska MJ, Hornbostel K, Kanstad T, Hendriks MA, Markeset G. Inspection and assessment of corrosion in pretensioned concrete bridge girders exposed to coastal climate. Infrastructures 2020;5(9):76–101. https://doi.org/10.3390/infrastructures5090076.

[7] Norwegian Public Roads Administration. Bridge Management System (BRUTUS) [Internet, in Norwegian].

[8] Martin RD, Kang T-H-K, Pei J-S. Experimental and code analyses for shear design of AASHTO prestressed concrete girders. PCI J 2011;56(1):54–74. https://doi.org/10.15554/pcij.01012011.54.74.

[9] ACI 318-05/318R-05 Building Code Requirements for Structural Concrete and Commentary. American Concrete Institute International. 2005.

[10] Murray CD, Cranor BN, Floyd RW, Pei J-S. Experimental testing of older AASHTO Type II bridge girders with corrosion damage at the ends. PCI J 2019;64(1):49–64. https://doi.org/10.15554/pcij64.1-02.

[11] Tanaka Y, Shimomura T, Yamaguchi T. Experimental and numerical study on the residual strength of deteriorated prestressed concrete bridge beams affected by chloride attack. In: Concrete Repair, Rehabilitation and Retrofitting III. CRC Press; 2012. p. 225–6.

[12] El Maaddawy T, Soudki K, Topper T. Long-term performance of corrosion-damaged reinforced concrete beams. ACI Struct J 2005;102(5):649–56. https://doi.org/10.14359/14660.

[13] Khan I, François R, Castel A. Experimental and analytical study of corroded shear-critical reinforced concrete beams. Mater Struct 2014;47(9):1467–81. https://doi.org/10.1617/s11527-013-0129-y.

[14] Ye Z, Zhang W, Gu X. Deterioration of shear behavior of corroded reinforced concrete beams. Eng Struct 2018;168:708–20. https://doi.org/10.1016/j.engstruct.2018.05.023.

[15] Fib Model Code for Concrete Structures 2010.

[16] Wang L, Zhang X, Zhang J, Yi J, Liu Y. Simplified model for corrosion-induced bond degradation between steel strand and concrete. J Mater Civ Eng 2017;29(4):04016257. https://doi.org/10.1061/(ASCE)MT.1943-5533.0001784.

[17] Cairns J, Plizzari GA, Du Y, Law DW, Franzoni C. Mechanical properties of corrosion-damaged reinforcement. ACI Mater J 2005;102(4):256–64.

[18] Du YG, Clark LA, Chan AHC. Residual capacity of corroded reinforcing bars. Mag Concr Res 2005;57(3):135–47. https://doi.org/10.1680/macr.2005.57.3.135.

[19] Apostolopoulos CA, Papadakis VG. Consequences of steel corrosion on the ductility properties of reinforcement bar. Constr Build Mater 2008;22(12):2316–24.

[20] Lee H-S, Cho Y-S. Evaluation of the mechanical properties of steel reinforcement embedded in concrete specimen as a function of the degree of reinforcement corrosion. Int J Fract 2009;157(1–2):81–8. https://doi.org/10.1007/s10704-009-9334-7.

[21] François R, Khan I, Dang VH. Impact of corrosion on mechanical properties of steel embedded in 27-year-old corroded reinforced concrete beams. Mater Struct 2013;46(6):899–910. https://doi.org/10.1617/s11527-012-9941-z.

[22] Du Y, Clark LA, Chan AHC. Impact of reinforcement corrosion on ductile behavior of reinforced concrete beams. ACI Struct J 2007;104(3):285–93. https://doi.org/10.14359/18618.

[23] Dang VH, François R. Prediction of ductility factor of corroded reinforced concrete beams exposed to long term aging in chloride environment. Cem Concr Compos 2014;53:136–47. https://doi.org/10.1016/j.cemconcomp.2014.06.002.

[24] Castel A, François R, Arliguie G. Mechanical behaviour of corroded reinforced concrete beams—Part 2: Bond and notch effects. Mater Struct 2000;33(9):545–51. https://doi.org/10.1007/BF02480534.

[25] Imperatore S, Rinaldi Z, Drago C. Degradation relationships for the mechanical properties of corroded steel rebars. Constr Build Mater 2017;148:219–30. https://doi.org/10.1016/j.conbuildmat.2017.04.209.

[26] Lu Z-H, Li F, Zhao Y-G. An investigation of degradation of mechanical behaviour of prestressing strands subjected to chloride attacking. Int Conf Durability Concr Struct 2016. https://doi.org/10.5703/1288284316111.

[27] Zhang X, Wang L, Zhang J, Liu Y. Corrosion-induced flexural behavior degradation of locally ungrouted post-tensioned concrete beams. Constr Build Mater 2017;134:7–17. https://doi.org/10.1016/j.conbuildmat.2016.12.140.

[28] Zeng Y-H, Gu X-L, Zhang W-P, Huang Q-H. Study on mechanical properties of corroded prestressed tendons [in Chinese]. J Build Mater 2010;13(2):169–74. https://doi.org/10.3969/j.issn.1007-9629.2010.02.008.

[29] Wang L, Li T, Dai L, Chen W, Huang K. Corrosion morphology and mechanical behavior of corroded prestressing strands. J Adv Concr Technol 2020;18(10):545–57. https://doi.org/10.3151/jact.18.545.

[30] Tu B, Dong Y, Fang Z. Time-dependent reliability and redundancy of corroded prestressed concrete bridges at material, component, and system levels. J Bridge Eng 2019;24(9):04019085. https://doi.org/10.1061/(ASCE)BE.1943-5592.0001461.

[31] Franceschini L, Vecchi F, Tondolo F, Belletti B, Montero JS. Mechanical behaviour of corroded strands under chloride attack: A new constitutive law. Constr Build Mater 2022;316:125872. https://doi.org/10.1016/j.conbuildmat.2021.125872.

[32] Jeon C-H, Lee J-B, Lon S, Shim C-S. Equivalent material model of corroded prestressing steel strand. J Mater Res Technol 2019;8(2):2450–60. https://doi.org/10.1016/j.jmrt.2019.02.010.

[33] Wang L, Yi J, Zhang J, Floyd RW, Ma Y. Bond Behavior of Corroded Strand in Pretensioned Prestressed Concrete Beams. ACI Struct J 2018;115(6):1803–12. https://doi.org/10.14359/51706892.

[34] Li F, Yuan Y. Effects of corrosion on bond behavior between steel strand and concrete. Constr Build Mater 2013;38:413–22. https://doi.org/10.1016/j.conbuildmat.2012.08.008.

[35] Wang L, Yi J, Zhang J, Jiang Y, Zhang X. Effect of corrosion-induced crack on the bond between strand and concrete. Constr Build Mater 2017;153:598–606. https://doi.org/10.1016/j.conbuildmat.2017.07.113.

[36] Yi J, Wang L, Floyd RW. Bond Strength Model of Strand in Corrosion-Induced Cracking Concrete. ACI Struct J 2020;117(6):119–32. https://doi.org/10.14359/51728060.

[37] Coronelli D, Gambarova P. Structural assessment of corroded reinforced concrete beams: modeling guidelines. J Struct Eng 2004;130(8):1214–24. https://doi.org/10.1061/(ASCE)0733-9445(2004)130:8(1214).

[38] Hanjari KZ, Kettil P, Lundgren K. Analysis of mechanical behavior of corroded reinforced concrete structures. ACI Struct J 2011;108(5):532–41.

[39] Nasser H, Van Steen C, Vrijdaghs R, Torres-Acosta AA, Vandewalle L, Verstrynge E. Numerical modelling of corroded reinforced concrete beams based on visual inspection. In Proceedings of SMAR Conference 2019; 2019: SMAR.

[40] Molina FJ, Alonso C, Andrade C. Cover cracking as a function of rebar corrosion: Part 2—Numerical model. Mater Struct 1993;26(9):532–48. https://doi.org/10.1007/BF02472864.

[41] Wang L, Dai L, Bian H, Ma Y, Zhang J. Concrete cracking prediction under combined prestress and strand corrosion. Struct Infrastruct Eng 2019;15(3):285–95. https://doi.org/10.1080/15732479.2018.1550519.

[42] Dai L, Wang L, Zhang J, Zhang X. A global model for corrosion-induced cracking in prestressed concrete structures. Eng Fail Anal 2016;62:263–75.

[43] Norwegian Public Roads Administration. Bridge Design-08: NIB - Bridges: norm [Handbook 100, in Norwegian]. 1st ed. 1983.

[44] Norwegian Standard NS 3473. Concrete structures - Design rules [in Norwegian]. 2nd issue, 2nd edition. 1982.

[45] Norwegian Standard NS 3473. Concrete structures - Design rules [in Norwegian]. 3rd issue. 1989.

[46] Norwegian Public Roads Administration. Bridge Design-08: NIB - Bridges: norm [Handbook 100, in Norwegian]. 2nd ed. 1989.

[47] Norwegian Standard NS 481-2:1968. Reinforcing steel - Hot rolled deformed bars [in Norwegian]. 1968.

[48] Norwegian Standard NS-EN 1992-1-1: 2004+ A1: 2014+ NA: 2018. Eurokode 2: Prosjektering av betongkonstruksjoner-Del 1-1: Allmenne regler og regler for bygninger [in Norwegian]. 2021.

[49] Norwegian Public Roads Administration. Classification of carrying capacity of bridges, loads [Handbook V412, in Norwegian]. 2021.

[50] Osmolska MJ, Kanstad T, Hendriks MAN, Markeset G. Corrosion assessment and effect on the structural performance of pretensioned bridge girders in coastal climate. Proceedings of the fib CACRCS DAYS. 2020.

[51] de Putter A, Hendriks MAN, Rots JG, Yang Y, Engen M, van den Bos AA. Quantification of the resistance modeling uncertainty of 19 alternative 2D nonlinear finite element approaches benchmarked against 101 experiments on reinforced concrete beams. Struct Concr 2022;1–15. https://doi.org/10.1002/suco.202100574.

[52] Dimensjonering av spennbetong: 29. januar - 1. februar 1980, Sandefjord [in Norwegian]. Norwegian Association of Civil Engineers; 1980.

[53] Eriksen M, Kolstad MT. Investigation of cracking behavior in reinforced concrete panels with bond-slip reinforcement. Master thesis. NTNU; 2016.

[54] Diana FEA guideline. https://dianafea.com/faq-tangent-normal-stiffness.

[55] AASHTO LRFD Bridge design specifications, 2nd ed. American Association of State Highway and Transportation Officials, Washington, DC. 1998.

[56] Abdelatif AO, Owen JS, Hussein MFM. Modelling the prestress transfer in pre-tensioned concrete elements. Finite Elem Anal Des 2015;94:47–63. https://doi.org/10.1016/j.finel.2014.09.007.

[57] Norsk Betongforening. Publikasjon nr. 3. Normerte I-tverrsnitt «NIB» [in Norwegian]. Oslo 1974.

[58] Verstrynge E. The Relation Between Concrete Crack Width and Rebar Corrosion Level Validated on a Large Set of Experimental Data. fib congress in Oslo, June 2022.

[59] Kioumarsi MM, Hendriks MAN, Kohler J, Geiker MR. The effect of interference of corrosion pits on the failure probability of a reinforced concrete beam. Eng Struct 2016;114:113–21. https://doi.org/10.1016/j.engstruct.2016.01.058.

[60] Floyd R, Pei J-S, Tang PF, Murray CD. Understanding the behavior of prestressed girders after years of service. Technical Report. Oklahoma Dept. of Transportation; 2016.

[61] Ma Y, Guo Z, Wang L, Zhang J. Probabilistic Life Prediction for Reinforced Concrete Structures Subjected to Seasonal Corrosion-Fatigue Damage. J Struct Eng 2020;146(7):04020117. https://doi.org/10.1061/(ASCE)ST.1943-541X.0002666.